mTOR inhibition in Q175 Huntington's disease model mice facilitates neuronal autophagy and mutant huntingtin clearance

Philip Stavrides[1], Chris N. Goulbourne[1], James Peddy[1], Chunfeng Huo[1], Mala Rao[1, 2], Vinod Khetarpal[5], Deanna M. Marchionini[5], Ralph A. Nixon[1, 2, 3, 4, #], Dun-Sheng Yang[1, 2, @]

[1]Center for Dementia Research, Nathan S. Kline Institute, Orangeburg, NY 10962 USA; Departments of [2]Psychiatry and [3]Cell Biology, and [4]NYU Neuroscience Institute, New York University Grossman School of Medicine, New York, NY 10016 USA; [5]CHDI Management/CHDI Foundation, New York, NY 10001 USA.

[@] Correspondence: Dun-Sheng.Yang@NKI.RFMH.ORG

[#] **Lead contact:**

Ralph A. Nixon, MD, PhD

Center for Dementia Research

Nathan S. Kline Institute

140 Old Orangeburg Road

Orangeburg, NY 10962

Phone: (845) 398-5423

Fax: (845) 398-5422

Email: Ralph.Nixon@NKI.RFMH.ORG

ABSTRACT

Huntington's disease (HD) is caused by expansion of the polyglutamine stretch in huntingtin protein (HTT) resulting in hallmark aggresomes/inclusion bodies (IBs) composed of mutant huntingtin protein (mHTT) and its fragments. Stimulating autophagy to enhance mHTT clearance is considered a potential therapeutic strategy for HD. Our recent evaluation of the autophagic-lysosomal pathway (ALP) in human HD brain reveals upregulated lysosomal biogenesis and relatively normal autophagy flux in early Vonsattel grade brains, but impaired autolysosome clearance in late grade brains, suggesting that autophagy stimulation could have therapeutic benefits as an earlier clinical intervention. Here, we tested this hypothesis by crossing the Q175 HD knock-in model with our autophagy reporter mouse TRGL (**T**hy-1-**R**FP-**G**FP-**L**C3) to investigate *in vivo* neuronal ALP dynamics. In the Q175 and/or TRGL/Q175 mice, mHTT was detected in autophagic vacuoles and also exhibited high level colocalization with autophagy receptors p62/SQSTM1 and ubiquitin in the IBs. Compared to the robust lysosomal pathology in late-stage human HD striatum, ALP alterations in Q175 models are also late-onset but milder that included a lowered phospho-p70S6K level, lysosome depletion and autolysosome elevation including more poorly acidified autolysosomes and larger-sized lipofuscin granules, reflecting impaired autophagic flux. Administration of a mTOR inhibitor to 6-mo-old TRGL/Q175 normalized lysosome number, ameliorated aggresome pathology while reducing mHTT-, p62- and ubiquitin-immunoreactivities, suggesting beneficial potential of autophagy modulation at early stages of disease progression.

KEY WORDS

Huntington's disease, Q175 mouse model, huntingtin, autophagy, TRGL, autophagy modulation

52 **INTRODUCTION**

53 Huntington's disease (HD) is an autosomal dominant disorder caused by a mutation in the
54 gene encoding the huntingtin protein (HTT) resulting in expansion of the polyglutamine (polyQ)
55 stretch on its amino-terminus [7, 18, 26, 68]. HD pathogenesis advances in a spatiotemporal
56 pattern, which is used to stage disease pathology severity as Grade 0-4 (HD0, HD1, HD2, etc.)[73].
57 GABA-containing medium spiny projection neurons in the striatum are most susceptible to cell
58 death [72], and the cerebral cortex, particularly layer 5a, also shows cell loss [55, 66]. Neuronal
59 intranuclear inclusions (NIIs) and neuropil inclusions are present in HD brains and are positive for
60 mutant huntingtin (mHTT) and ubiquitin (Ub) [17, 20].

61 Recently, we completed a comprehensive evaluation of the autophagic-lysosomal pathway
62 (ALP) in the HD brain at progressive disease stages, focusing on the most affected brain region,
63 the striatum, in comparison to a less affected region, the neocortex [9]. Double fluorescence
64 immunolabeling and immuno-electron microscopy (IEM) revealed colocalization of HTT/mHTT
65 with the autophagy-related adaptor proteins, p62/SQSTM1 and ubiquitin, and cathepsin D (CTSD)
66 within aggresome inclusions and autophagic compartments, documenting the involvement of ALP
67 in HTT/mHTT turnover and the disease-related impairment of this process in late-stage disease.
68 The temporal evolution of ALP alterations generally revealed minimal detectable impairment of
69 upstream autophagy steps [e.g., autophagosome (AP) induction, formation, and fusion with
70 lysosomes (LY)] and, in striatum, elevated levels of LAMP1 and LAMP2 markers suggesting
71 modestly upregulated LY biogenesis. At late disease stages, mainly HD4, neuronal ALP
72 dysfunction exhibited enlarged/clumped CTSD-immunoreactive autolysosomes (AL)/LY and
73 ultrastructural evidence of autophagic vacuole (AV) fusion and transition to lipofuscin granule
74 formation. These findings collectively suggest that a relatively competent autophagy machinery
75 is maintained during the disease progression with a compensatory upregulation in lysosomal
76 biogenesis, which together prevents against mHTT accumulation. This situation is failing at the
77 late disease stages when AL clearance is impeded, substrates, including mHTT and its metabolites,
78 accumulate in AL and aggresome inclusions increase.

79 A possible implication of the foregoing findings is that pharmacologic enhancement of
80 autophagy applied at a symptomatic but early stage of disease, when the ALP clearance machinery
81 is fully competent, may be therapeutic in clearing mHTT protein in affected neurons. By contrast,

82 in Alzheimer's Disease (AD) lysosomal clearance deficits develop at the earliest disease stages,
83 suggesting enhanced autophagy induction is counterproductive.

84 Modulation of autophagy as a therapeutic strategy for HD has been investigated in various
85 cell and animal models of HD [11, 26, 28, 64, 77]. Of particular relevance to our present study are
86 those involving autophagy induction with mTOR-dependent or -independent autophagy-
87 enhancing approaches in HD mouse models [e.g. Trehalose [67]; Rapamycin analog Temsirolimus
88 (CCI-779) [57]; Rilmenidine [59]; Rhes manipulations [5, 35]]. These studies have generally
89 demonstrated ameliorative effects on outcome measures such as mHTT lowering and
90 behavioral/motor function assays. However, in many cases it is unclear whether autophagy
91 mechanisms are directly engaged in the brain or are critical to rescue.

92 Thus, our study aimed to comprehensively characterize the autophagy response with a range
93 of autophagy markers to interrogate the competence of the entire autophagy process in relationship
94 to mHTT in the well-characterized zQ175 Knock-In HD mouse model (Q175). Towards this goal,
95 we evaluated autophagy in neurons of Q175 after introducing by neuron-specific transgenesis the
96 dual fluorescence-tagged autophagy probe, **t**andem **f**luorescent mRFP-eGFP-**LC3** (tfLC3), an
97 autophagy adaptor protein associated with AP and metabolized via autophagy [34]. We thereby
98 generated a new Q175 cross, namely TRGL (**T**hy-1-**R**FP-**G**FP-**L**C3)/Q175. tfLC3 expression,
99 driven postnatally by the neuron-specific Thy1-promoter, allows for selective monitoring of
100 neuronal autophagy without the confounding influence of glial cells. Resolution and sensitivity in
101 reporting tfLC3 signal is high compared to conventional immunofluorescence staining of LC3.
102 The ability to ratiometrically report pH-dependent changes in fluorescence wavelength (hue angle)
103 enables neutral pH AP to be distinguished from acidic AL, that progressively acidify
104 intraluminally upon fusion with LY. We are further able to differentiate AL subgroups differing
105 in their extent of acidification after LY fusion. Distinguishing properly acidified AL from those
106 poorly acidified because of delayed or defective acidification is assisted by immunolabeling AL
107 with a marker, such as cathepsin D, which is then detected with a third fluorophore. Together this
108 triple fluorescence paradigm objectively quantified by computer-assisted deconvolution of the
109 proportions of each label within the analyzed neuron, a reflection of their relative pH (and fusion
110 with LY), which allows ALP organelle subtypes including LC3-nagative LY to be identified and
111 quantified for their numbers, sizes and spatial distributions in intact brain sections. The collective
112 data provides reports on the completion (or lack thereof) of autophagy flux (ALP dynamics) and

113 any blockage at particular steps in the ALP pathway, including the normal acidification and further
114 maturation of AL through their successful elimination of fluorescence-tagged LC3 [34, 36, 38,
115 39].

116 Crossing TRGL mice with a model of a neurodegenerative disease, the Q175 mouse model
117 of HD, has enabled us to assess disease-related autophagy alterations in the Q175 and TRGL/Q175
118 models and their response to a pharmacological inhibition of mTOR, (mTORi) INK-128 (hereafter
119 INK). Our data demonstrate target engagement and positive effects of the compound on rescuing
120 Q175 phenotypes including reversal on AL/LY subtypes as reported by the tfLC3 probe and
121 parallel reductions of mHTT-, p62- and Ub-immunoreactivity (IR), suggesting that the compound
122 targeted the ALP to degrade mHTT.

123

124

125 **MATERIALS AND METHODS**

126 ***The HD Q175 mouse model and the generation of a new Q175 model crossed with the autophagy***
127 ***reporter mouse TRGL (TRGL/Q175)****:* Q175 mice (B6J.zQ175 Knock-In mice, CHDI-
128 81003003)[45, 46] were obtained from the Jackson Lab (Stock No. 027410) on a C57BL/6J
129 background. The zQ175 KI allele has the mouse *Htt* exon 1 replaced by the human *HTT* exon 1
130 sequence containing a ~190 CAG repeat tract, and the average size for the mice used in this study
131 was 200 CAG. Q175 genotyping and CAG sizing were conducted by Laragen, Inc. (Culver City,
132 CA). The TRGL (**T**hy-1 m**R**FP-e**G**FP-**L**C3) mouse model, expressing tandem fluorescence-
133 tagged LC3 (tfLC3 or mRFP-eGFP-LC3) in neurons, was generated, genotyped by PCR and
134 maintained in a C57BL/6J background as described previously [34]. The TRGL was crossed with
135 Q175 to generate the new TRGL/Q175 model featuring the tfLC3 probe as an *in vivo* autophagy
136 reporter.

137 The mice were maintained in the Nathan Kline Institute for Psychiatric Research (NKI)
138 animal facility and housed in a 12 hrs light/dark cycle. All animal procedures were performed
139 following the National Institutes of Health Guidelines for the Humane Treatment of Animals, with
140 approval from the Institutional Animal Care and Use Committee at the NKI. Animals of both sexes
141 were used in this study. Details for mouse ages are in the Figure Legend and/or Results. All efforts
142 were made to minimize animal suffering and number of animals used.

143

144 ***mTORi INK administration to mice**:* INK-128 (ChemScene) was formulated in the sterile filtered
145 vehicle (Veh) – 0.5% carboxymethyl cellulose (Sigma, Cat #5678) and 0.05% tween 80 in water
146 – at different concentrations to achieve the various desired dosages. The mixture was homogenized
147 with a tissue homogenizer, stored in a sterile container at room temperature for up to 2 weeks, and
148 stirred prior to each dosing. It was administered to mice via oral gavage at a dose volume of 5
149 ml/kg, which was a relatively smaller volume of drug solution (generally 100-150 ul depending
150 on the mouse body weight) aimed at avoiding the suppression of appetite. Mice receiving the Veh
151 (also at a solution volume of 5 ml/kg) served as the control group. Oral gavage was conducted
152 with 20G-38mm Cadence Science™ Malleable Stainless-Steel Animal Feeding Needles #9921
153 (Fisher Sci Cat #.14-825-275).
154
155 ***mTORi INK pharmacokinetics in mouse brains after oral administration:*** INK was formulated
156 into 0.5% carboxymethyl cellulose and 0.05% tween-80 in water to be administered orally. 6
157 months old C57B6/J male mice were treated with compound at 1, 3 or 10 mg/kg (mpk) or vehicle.
158 6, 12 or 24 hours after administration, mice were terminally anesthetized with pentobarbital and
159 cerebellum was dissected and fresh frozen on liquid nitrogen and stored at -80ºC until analysis.
160 Tissue was homogenized and extracted with acetonitrile (containing 0.1% formic acid). Extract
161 was analyzed using a LC-MS/MS (Waters Xevo TQ MS) method with a lower limit of quantitation
162 of 13 nM.
163
164 ***Brain tissue preparation**:* To obtain tissues for experiments, the animals were anesthetized with a
165 mixture of ketamine (100 mg/kg BW) and xylazine (10 mg/kg BW). Mice for light microscopic
166 (LM) analyses were usually fixed by cardiac perfusion using 4% paraformaldehyde (PFA) in 0.1
167 M sodium cacodylate buffer [pH 7.4, Electron Microscopy Sciences (EMS), Hatfield, PA].
168 Following perfusion fixation, the brains were immersion-fixed in the same fixative overnight at
169 4°C. For transmission electron microscopic (EM) study, 4% PFA was supplemented with 2%
170 glutaraldehyde (EMS). For biochemical analyses such as immunoblotting, the brains were flash
171 frozen on dry ice and stored at –70°C. When both morphological and biochemical analyses were
172 to be performed on the same brain, the brain was removed after brief perfusion with saline. One
173 hemisphere was frozen at –70°C and the other half was immersion-fixed in 4% PFA for 3 days at
174 4°C.

175

176 ***Antibodies for immunohistochemistry (IHC) and western blotting (WB):*** The following primary
177 antibodies were used in this study. (1) from Cell Signaling Technology: tHTT rabbit mAb (total
178 HTTs, #5656), MTOR rabbit mAb (#2983); p-MTOR (S2481 autophosphorylation) pAb (#2974),
179 p-MTOR (S2448) pAb (#2971), p70S6K rabbit mAb (#2708), p-p70S6K (S371) pAb (#9208), p-
180 p70S6K (T389) rabbit mAb (#9235), S6 ribosomal protein mAb (#2317), p-S6 ribosomal protein
181 (S240/244) rabbit mAb (#5364), ULK1 pAb (#4773), ULK1 rabbit mAb (#6439), p-ULK1 (S757)
182 pAb (#6888), p-ULK1 (S317) pAb (#37762), ATG5 rabbit mAb (#12994), ATG14 pAb (#5504),
183 p-ATG14 (S29) rabbit mAb (#92340), p-Beclin 1 (S30) rabbit mAb (#35955), VPS34 rabbit mAb
184 (#4263), TRAF6 rabbit mAb (#8028). (2) from Millipore-Sigma: ntHTT mAb (mEM48,
185 #MAB5374; N-Terminus-specific), HTT mAb (1C2, #MAB1574; epitope: N-terminal part of the
186 human TATA Box Binding Protein (TBP) containing a 38-glns stretch), HTT mAb (#MAB5490;
187 epitope: human HTT aa115-129), ATG5 pAb (#ABC14), LC3 pAb (#ABC929), β–actin mAb
188 (#A1978). (3) from other vendors: HTT mAb MW8 (epitope: HD exon 1 with 67Q; Develop
189 Studies Hybridoma Bank, University of Iowa), HTT mAb PHP2 (CHDI-90001516-2,
190 Coriell/CHDI), Beclin 1 mAb (BD Biosciences, #612113), LC3 pAb (Novus Biologics, #NB100-
191 2220), p62/SQSTM1 mAb (BD Biosciences, #610832) or C-term-specific p62/SQSTM1 Guinea
192 Pig pAb (Progen Biotechnik #C-1620); ubiquitin pAb (Dako Agilent, #Z0458), ubiquitin pAb
193 (Abcam, #ab7780), LAMP1 rat mAb (Developmental Studies Hybridoma Bank, #H4A3), CTSB
194 goat pAb (Neuromics, #GT15047). (4) In-house made: CTSD pAb (RU4). CTSD sheep pAb (D-
195 2-3)[13].

196 The following secondary antibodies and reagents for immunoperoxidase labeling were
197 purchased from Vector Laboratories (Burlingame, CA): biotinylated goat anti-rabbit or -mouse
198 IgG/IgM, Vectastain ABC kit (PK-4000), and DAB Peroxidase Substrate Kit (SK-4100). Mouse
199 on Mouse (M.O.M) detection kit (BMK-2201), normal-goat (S-100) and normal-donkey (S-2000-
200 20) serum blocking solution were also from Vector Lab. The following secondary antibodies for
201 immunofluorescence were purchased from Thermo Fisher Scientific (Waltham, MA): Alexa Fluor
202 488-conjugated goat anti-rabbit IgG (A11034), Alexa Fluor 568- goat anti-rabbit IgG (A11036),
203 Alexa Fluor 647- goat anti-rabbit (A21245), Alexa Fluor Plus 405- goat anti-rabbit (A48254),
204 Alexa Fluor 568- goat anti-mouse IgG (A11031), Alexa Fluor 647- goat anti-mouse (A21235) and
205 Alexa Fluor 647- goat anti-rat (A21247). HRP- linked secondary antibodies for immunoblotting

206 were obtained from Jackson ImmunoResearch Laboratories (West Grove, PA): Rabbit IgG (711-
207 035-152), Mouse IgG (711-035-150), Rat IgG (712-035-150), and Goat IgG (705-035-003).
208
209 ***Immunolabeling of brain sections:*** Immunoperoxidase and immunofluorescence IHC were
210 performed according to the protocols previously described [34, 76]. Brain vibratome sections (40
211 μm) were blocked and incubated in primary antibody O/N (up to 3 days in some cases) at 4°C.
212 ABC detection method was used for immunoperoxidase labeling visualized with DAB while
213 Alexa-Fluor conjugated secondary antibodies were used for immunofluorescence.
214 Autofluorescence was quenched with 1% Sudan black (Sigma-Aldrich; St. Louis, MO) in 70%
215 ethanol for 20 minutes. DAB labeled sections was inspected on a Zeiss AxioSkop II equipped with
216 a HrM digital camera (Carl Zeiss, Germany). Immunofluoescently labeled sections were examined
217 on a Zeiss LSM880 confocal microscope.
218
219 ***Confocal image collection and hue-angle based quantitative analysis for AV/LY subtypes:***
220 Confocal imaging was performed using a plan-Apochromat 20x or 40x/1.4 oil objective lens on a
221 LSM880 laser scanning confocal microscope with the following parameters: eGFP (ex: 488, em:
222 490-560 with MBS 488), mRFP (ex: 561, em: 582-640 with MBS 458/561), Alexafluor 647 (ex:
223 633, em: 640-710 with MBS 488/561/633) and DAPI (ex: 405, em: 410-483), with the 'best signal
224 scanning mode' which separates scanning tracks for each excitation and emission set to exclude
225 crosstalk between each fluorophore signal. The resolution of 40x images was 1024 x 1024 pixels
226 (corresponding to an area of 212.34 x 212.34 μm^2), and the resolution of 3x digitally zoomed
227 images was also 1024 x 1024 pixels (corresponding to an area of 70.78 x 70.78 μm^2). Detailed
228 settings for image collection were reported previously [34].
229 Hue angle-based vesicle analysis enables quantitative determination of AV/LY subtypes
230 including AP, AL, poorly acidified AL (pa-AL) and pure LY and the method was described in
231 detail previously [34]. Briefly, high resolution confocal images containing the LC3 (red and green)
232 and CTSD (blue) punctate signals were analyzed with the Zen Blue Image Analysis Module from
233 Carl Zeiss Microscopy. Threshold for each of the three-color channels (red, green, blue; RGB) was
234 set by taking the average of intensity value from 20 neuronal perikarya. The signal was segmented
235 into discrete puncta by using the automatic watershed function to separate clumped vesicles into
236 individual puncta. Background signal was eliminated using the size exclusion function of Zen

237 Blue. The R, G and B intensity values of each vesicle were calculated using the profile function of
238 Zen Blue. The RGB ratio of each vesicle was converted into a hue angle and saturation range –
239 which we assigned to each AV subtype and should match the desired AV color range as perceived
240 visually (i.e., yellow for AP, blue for Ly, purple for AL and white for de-acidified AL) – by
241 entering the values of R, G, and B for a given punctum into the formula, as follows: Hue° =
242 IF(180/PI()*ATAN2(2*R-G-B,SQRT(3)*(G-B)) < 0,180/PI()*ATAN2(2*R-G-B,SQRT(3) *(G-
243 B)) + 360,180/PI()*ATAN2(2*R-G-B,SQRT(3)*(G-B))). Saturation percent of the hue angle was
244 calculated by entering the values of R, G, and B for a given punctum into the following formula =
245 (MAX(RGB)-MIN(RGB))/SUM(MAX(RGB)+MIN(RGB))*100 (www.workwithcolor.com),
246 provided lightness is less than 1, which is the usual case for our data. Hue angle was converted to
247 color using the Hue color wheel. The data was pooled and categorized in Excel spreadsheets.
248
249 ***Ultrastructural analyses:*** Vibratome brain sections (50 µm) were treated with 1% osmium
250 tetroxide in 100 mM sodium cacodylate buffer pH 7.4 for 30 minutes, washed in distilled water
251 four times (10 min/wash), and then treated with 2% aqueous uranyl acetate overnight at 4°C in the
252 dark. Samples were then washed and sequentially dehydrated with increasing concentrations of
253 ethanol (20, 30, 50, 70, 90, and 100%) for 30 min each, followed by three additional treatments
254 with 100% ethanol for 20 min each. Samples were then infiltrated with increasing concentrations
255 of Spurr's resin (25% for 1 h, 50% for 1 h, 75% for 1 h, 100% for 1 h, 100% overnight at room
256 temperature), and then incubated overnight at 70°C in a resin mold. For TEM ultrastructural
257 analysis, 70 nm sections were cut using a Leica Reichert Ultracut S ultramicrotome and a Diatome
258 diamond knife, placed on to grids and then post stained with 2% uranyl acetate and lead citrate.
259 Images were taken using a Ceta Camera on a ThermoFisher Talos L120C transmission electron
260 microscope operating at 120kV.
261 For post-embedding IEM, ultrathin sections were placed on to carbon formvar 75 mesh
262 nickel grids and etched using 4% sodium metaperidotate for 10 minutes before being washed twice
263 in distilled water and then blocked for one hour. Grids were incubated in the primary antibodies at
264 4 °C overnight. Next day grids underwent seven washes in 1xPBS and were then incubated in anti-
265 mouse or anti rabbit 10 nm gold secondary (1/50 dilution) for 1 hour. After this the grid was
266 washed seven times in 1xPBS and twice in distilled water. Grids were then silver enhanced for 5
267 minutes (Nanoprobes). Grids were finally post stained with 1% uranyl acetate for 5 minutes

268 followed by two washes in water and then stained with lead citrate for 5 minutes followed by a
269 final two washes in distilled water. Samples were then imaged on a ThermoFisher Talos L120C
270 operating at 120kV.
271
272 ***Western blotting**:* Samples for WB were prepared by homogenizing brains in a tissue-
273 homogenizing buffer (250 mM sucrose, 20 mM Tris pH 7.4, 1 mM EDTA, 1 mM EGTA)
274 containing protease and phosphatase inhibitors as previously described. [65] Following
275 electrophoresis, proteins were transferred onto 0.2 µm-pore nitrocellulose membranes (Whatman,
276 Florham Park, NJ) at 100 mA for 8-12 hours depending on the target protein. The blots were
277 blocked for 1 hour in 5% non-fat milk in TBS, rinsed in TBST (TBS + 0.1% Tween-20), then
278 incubated with a primary antibody in 1% BSA/TBST overnight at 4°C. The membrane was washed
279 and incubated in a HRP conjugated goat-anti rabbit or mouse secondary antibody, diluted 1:5000
280 in 5% milk for 1 hr at room temperature. The membrane was again washed and then incubated in
281 a Novex ECL (Invitrogen) for 1 min. The detection of the signals was achieved through either
282 exposure to a film or scanning by a digital gel imager (Syngene G:Box XX9) as specified in the
283 figure legends. Densitometry was performed with Image J and the results were normalized by the
284 immunoblot(s) of given loading control protein(s) (usually GAPDH, unless otherwise noted).
285
286
287 **RESULTS**
288 **Identification of inclusions and HTT molecular species in Q175 mice**
289 Immunohistochemistry (IHC) experiments with the antibody mEM48, which preferentially
290 recognizes aggregated mHTT [20], revealed age-dependent development of mHTT-positive
291 profiles in the striatum of Q175KI mice. Brain sections from 2.5-mo-old Q175 (not shown) only
292 exhibited faint and diffuse nuclear mHTT staining without identifiable aggresomes/inclusion
293 bodies (IBs), while at 6 and 10 months of age, mHTT-positive IBs were readily detected
294 progressively with age (Fig. 1A2-A3). There were no similar mHTT immunoreactive puncta in
295 WT striatum (Fig. 1A1). These observations are consistent with previous findings in Q175 and
296 other HD mouse models [12, 37, 46]. To further determine the locations of mHTT IBs in Q175,
297 mEM48-immunostained sections were counterstained with cresyl violet (Fig. 1A4) to distinguish
298 nuclear IBs (Fig. 1A4, arrowheads) from extranuclear IBs, which were localized predominantly in

299 the neuropil (Fig. 1A4, arrows) and also detected rarely in the cytoplasmic portion of the
300 perikaryon. Thus, our results demonstrate age-dependent increase in mHTT aggresomes in the
301 Q175 model.

302 To reveal the ultrastructural locations and features of the mHTT aggregates, immunogold
303 EM (IEM) with antibody mEM48 was performed. EM images (Fig. 1B) demonstrated that the IEM
304 with this antibody was highly specific in detecting mHTT IBs which were localized in the neuronal
305 nuclei, dendrites and axons. Ultrastructurally, most IBs were cotton-ball shaped and composed of
306 fine fibrous or granular elements, somewhat similar to the unbundled short fibrils/protofibrils
307 found *in vitro* with recombinant mHTT protein fragments [32, 33, 42], and similar to the structure
308 of NII type inclusions we found in the human HD brain [9]. Notably, however, human neuritic IBs
309 often displayed a more heterogeneous composition, such as fine fibrils mixed with AVs or bundles
310 composed of microtubule-like filaments, which were not found in the mouse neuritic IBs. Thus,
311 the result suggests a homogenous aggresome pathology in the mouse model, possible reflecting a
312 more rapid formation rate than in human.

313 Previous immunoblotting studies have observed fragmentation of mHTT molecules in the
314 human brain [30, 47], including our own study which detects mHTT fragments of 45-48 kDa,
315 which predominantly exist in HD striatum [9]. To assess HTT molecular species in the Q175
316 mouse brain, we employed multiple antibodies that preferentially detected mHTT over wild type
317 HTT, including MAB1574 (Clone 1C2) (Fig. 1C1, C2), its epitope containing a 38-glns stretch
318 [69], and mAb PHP2 (Fig. 1C1), reacting with the peptide sequence QAQPLLPQP within the
319 proline rich domain of HTT [32]. Both detected full-length mHTT and a ~120 kDa fragment in the
320 Q175 model (Figs. 1C1; 1C2 left and 1C3 top two graphs). By contrast, MAB5490 (Fig. 1C2
321 right), reacting with aa115-129 of HTT (C-terminal to the region of polyQ stretch-containing exon
322 1), detected both wild type and mutant forms of HTT (Fig. 1C3, bottom right graph). A ~48 kDa
323 HTT fragment may correspond to the 45-48 kDa fragment seen in human brain [9], and was
324 detected by both MAB1574 and MAB5490 antibodies in some samples (Fig. 1C2) but its levels in
325 the Q175 models and the control TRGL were not statistically significantly different (Fig. 1C3,
326 bottom left graph). Thus, the result suggests that HTT fragmentation is not obvious in the Q175
327 brains, unlike the far more prevalent occurrence of this phenomenon in human HD striatum.
328

329 **mHTT colocalizes with p62, Ub and CTSD in Q175 striatum**

330 Our earlier study in human HD brains [9] found a high degree of colocalization of mHTT/Ub
331 or Ub/p62 colocalized signals in IBs, suggesting a relationship between mHTT and the autophagy
332 machinery since p62 and Ub are adaptor proteins mediating autophagic cargo sequestration.
333 Similarly, in Q175 mice, mHTT/Ub or Ub/p62 signals were highly colocalized in IBs, particularly
334 in NIIs, in striatal neurons of Q175 mice (Fig. S1). Additional triple IF labeling experiments
335 (mHTT/Ub/p62) with brain sections from 6- and 10-mo-old Q175 mice identified IBs positive for
336 mHTT, p62 and Ub within or outside the nuclei (Fig. 2A, arrows and arrowheads, respectively).
337 The 10-mo-old Q175 mice exhibited more and larger mHTT-positive IBs than 6-mo mutants (Fig.
338 2A, 1st column), consistent with Fig. 1A and the literature [12, 16]. Thus, our data demonstrate a
339 close spatial relationship among mHTT and autophagy receptor protein p62 and Ub in the Q175
340 model, which is consistent with our observations in human HD brain [9].
341 Double IF labeling of mHTT with a LY marker cathepsin D (CTSD) (Fig. 2B1) detected
342 small punctate mHTT signal in CTSD-positive vesicles, suggesting a pool of mHTT within the
343 ALP. Consistent with this light microscopic (LM) finding, IEM with antibody MAB1574 directed
344 against mHTT clearly demonstrated that the AVs in either cell bodies, dendrites and axons were
345 labeled with concentrated silver-enhanced gold particles (Fig. 2B2), and the specificity of the IEM
346 labeling was very high, as reflected by a much higher number of silver-enhanced gold particles
347 associated with AVs versus the minimal number of silver-enhanced gold particles with
348 mitochondria that represent the background labeling (Fig. 2B3). Together, the LM and IEM
349 findings suggest that mHTT molecules exist within ALP vesicles in the absence of definable
350 aggresome/IB structures, similar to the IEM finding from a recent report [78].
351
352 **Mild late-onset alterations in the ALP revealed in 17-mo-old Q175 mice**
353 We crossed TRGL mice [34] with Q175 to generate TRGL/Q175 and assessed AV/LY
354 subtypes in striatal neurons with a hue angle-based analysis method [34, 36]. Our pilot studies in
355 young TRGL/Q175 mice (2.5 to 6-mo of age) hardly detected autophagy alterations, compared to
356 the control TRGL mice (not shown). Previous studies have reported that autophagy impairment
357 was hardly detected in 6-mo Q175/GFP-LC3 mice [74], but alterations in a limited number of
358 autophagy markers (e.g., protein levels of p62, LC3, p-Beclin-1) were found in brain homogenates
359 of 12-15-mo Q175 mice [1, 21, 74]. Therefore, to further validate the status of the ALP and to

360 discover potential additional autophagy alterations, we expanded our study to old mice at 17-mo
361 of age, where we found the following ALP alterations.
362
363 ***(1) Alterations in AV/LY subtypes.*** Confocal images from 17-mo-old TRGL/Q175 and control
364 TRGL brain sections, triple-fluorescent labeled via an additional immunostaining with an anti-
365 CTSD antibody and far-red emitting fluorophore, showed enhanced mRFP- and eGFP-LC3 signals
366 in the striatal neurons of TRGL/Q175 compared to TRGL (Fig. 3A1). Hue angle-based analysis
367 confirmed the above observations by revealing significant increases in the numbers of AL and
368 poorly-acidified AL (pa-AL, as explained in Lee et al., 2019; 2022). It also detected a reduction in
369 the number of LY (Fig. 3A2). Thus, these results indicate that the tfLC3 reporter can reveal
370 alterations in the proportions of AV/LY subtypes in Q175, consistent with delayed and/or deficient
371 acidification of AL causing deficits in the reformation of LY to replenish the LY pool.
372
373 ***(2) Mild alterations in the levels of autophagy marker proteins detected by immunoblotting.*** To
374 further assess autophagy phenotypes in Q175 models, we conducted western blotting (WB) using
375 hemibrain homogenates from 17-mo-old mice for protein markers of individual steps in the ALP
376 (i.e., autophagy induction, membrane nucleation/AP formation, autophagy adaptor proteins and
377 AL formation/substrate degradation) (Fig. S2). At the stage of autophagy induction signaling, we
378 did not see alterations in the levels of mTOR and p-mTOR forms including its auto-phospho-form
379 at S2481, but we did observe a decreased level of a mTOR substrate, p-p70S6K (T389), in
380 TRGL/Q175 compared to the control TRGL (Fig. S2A), implying reduced mTOR activity, similar
381 to the finding from a previous study [57]. Another mTOR substrate, p-ULK1 (S757), did not
382 exhibit changes in TRGL/Q175. However, there was an increase in the level of total ULK1,
383 resulting in a reduced ratio of p-ULK1 (S757)/total ULK1 in TRGL/Q175 compared to TRGL
384 (Fig. S2A). The data collectively imply a down-regulated mTOR activity, as expected in response
385 to accumulated aggregate-prone protein in Q175 mice, or as a result of sequestration of mTOR by
386 mHTT IBs as suggested previously [57].
387 Except for these alterations, we did not detect statistically significant differences between
388 TRGL/Q175 and the control TRGL in all other tested marker proteins in the downstream phases
389 of the ALP (Fig. S2B-D). Of special interest is the ATG14-containing VPS34/Beclin-1 complex
390 implicated in HD pathogenesis [52, 74] for which we did not detect statistically significant

391 alterations in the levels of Beclin-1, VPS34 and ATG14 and their corresponding phosphor-forms.
392 Notably, even if some TRGL/Q175 clearly exhibited diminished signals for p-ATG14 (S29) (Fig.
393 S2B), no statistical significance could be established due to large variations among samples (See
394 Discussion). Another notable point is that we did not find alterations in levels of full-length
395 proteins or fragments [25, 49, 62, 70] of autophagy adaptor protein such as p62, TRAF6 (Fig.
396 S2C), in contrast to our immunoblot analysis of human HD brains [9]. Together, our data suggest
397 that, in general, autophagy alterations at the protein level, as can be detected by immunoblotting,
398 are mild in TRGL/Q175 even at 17-mo-old (See Discussion).
399
400 ***(3) Increased numbers of larger lipofuscin granules.*** To assess possible ultrastructural
401 pathologies, we conducted EM study for Q175 vs WT at 17-mo of age. As predicted, NIIs were
402 not observed in WT neurons (Fig. 3B, left panel) but were detected (Fig. 3B, right panel, red circle)
403 in ~10% striatal neurons of Q175 mice. Different from the substantial accumulation of AVs
404 including lipofuscin granules in late stage human HD brain (e.g., HD4) [9], we did not observe
405 gross accumulation of AVs in Q175 at this old age, except that quantitative analysis of EM images
406 revealed that larger sized (>1 μm) lipofuscin granules (Fig. 3B, right panel, arrow) modestly
407 increased in number in Q175 compared to WT [WT: 113 lipofuscin/420 neurons (n = 6 mice), i.e.,
408 27 lipofuscin/100 neurons; Q175: 228 lipofuscin/586 neurons (n = 9 mice), i.e., 39 lipofuscin/100
409 neurons; Unpaired t-test, Two-tailed P value < 0.01; Bar graph not shown]. Thus, these EM
410 findings suggest that ultrastructural autophagy alterations in the ALP were mild in Q175 even at
411 an older age.
412
413 **DARPP-32-IR decreases in striatal neurons of 17-mo-old TRGL/Q175 in the absence**
414 **neuronal loss**
415 To investigate potential neurodegeneration in our model, brain sections from 17-mo-old mice
416 were double-labeled with the medium spiny neuron marker DARPP-32 (dopamine- and cAMP-
417 regulated phosphoprotein, 32 kDa)[51] and a general neuronal marker NeuN. We found that the
418 intensity of DARPP-32-IR significantly diminished in TRGL/Q175 compared to TRGL (Fig. 4A,
419 B). However, there were no alterations in NeuN-IR, including Area Covered and the Number of
420 NeuN-positive neurons (Fig. 4A, B), and there were clear examples of neurons showing strong
421 NeuN signal but faint or no DARPP-32 signal (Fig. 4A, arrows). Such a finding is consistent with

422 other studies in Q175 and Q140 mice where neuronal loss was not found even though a reduction
423 in DARPP-32 was seen in the same study, and that neuronal loss only occurred quite late, e.g.,
424 around 2 years of age [16, 22, 53, 60]. Thus, our data support the notion that changes in DARPP-
425 32 may indicate alterations in its protein level and a loss of phenotype pattern, which is a
426 potentially common prelude to neuronal loss in other neuronal cell types, e.g., basal forebrain
427 cholinergic neurons [27].
428

429 **Oral mTORi INK engages mTOR target and induces downstream responses in the ALP in**
430 **7-mo-old TRGL/Q175**

431 As a prelude to investigate effects of pharmacological autophagy stimulation with a mTORi,
432 INK, on TRGL/Q175 mice, we first performed a safety, pharmacokinetic and pharmacodynamic
433 evaluation of INK in 6-mo-old WT mice, administered via oral gavage. The WB results (Fig. S3A)
434 indicated that all doses tested, from 2.5 mg/kg (mpk) to 10-mpk, exhibited target engagement as
435 revealed by the reductions in the protein levels of mTOR targets, i.e., p-ULK1 (S757,
436 phosphorylated by mTOR), p-p70S6K (not shown) or phosphorylated S6 ribosomal protein (p-S6,
437 at S240/244), implying high BBB permeability of this compound and target engagement.
438 Consistently, measurements for the levels of INK in cerebellar homogenates of WT mice treated
439 with 1, 3 and 10-mpk INK revealed dose-dependent brain levels of INK (Fig. S3B).

440 We then decided an oral gavage treatment regimen for INK as 4-mpk, daily, for 3 weeks, to
441 be administered in 6-mo-old TRGL/Q175. The brains from the mice (7-mo of age after the 3-week
442 treatment duration) were then analyzed by multiple experimental approaches. By immunoblotting,
443 target engagement was verified, as indicated by decreased levels of p-mTOR (S2481,
444 autophosphorylation site), p-ULK1 (S757) and p-S6 (S240) in brain homogenates from INK-
445 treated TRGL/Q175 compared to Veh-treated TRGL/Q175 (Fig. 5A, B). Additionally, there were
446 also INK induced changes in marker proteins located downstream of autophagy induction,
447 including, for example, increased levels of p-ATG14 in INK-treated samples (Fig. 5A, B). It is
448 interesting that although INK did not induce any alterations in the transgene product tfLC3-I or -
449 II, there was a trend of decreased endogenous LC3-I, leading to a statistically significant increase
450 in the ratio of LC3-II/I, and such a result in LC3-I reduction was reproduced in a repeated
451 experiment (Fig. 5A, B). Thus, the pilot study in WT mice and the actual study in TRGL/Q175

452 mice together established mTORi INK's BBB permeability, target engagement and ability to
453 modify molecular events in the ALP.
454
455 **mTOR inhibition alters AV/LY subtypes**
456 We took advantage of the tfLC3 construct reporting *in vivo* autophagy flux [34] to assess
457 INK effects on AV/LY subtypes in TRGL/Q175. Confocal images from INK- or Veh-treated
458 TRGL/Q175 and Veh-treated TRGL brain sections of 7-mo-old mice, immuno-stained with anti-
459 CTSD antibody and detected with a third fluorophore, were collected (Fig. 6A) and processed for
460 hue-angle based quantitative analysis using the protocol described previously [34]. The analysis
461 in striatal neurons (Fig. 6B) revealed reversal of the two main ALP alterations. First, the pre-
462 existing abnormally lowered LY number in TRGL/Q175-Veh (Fig. 6B, LY group, red vs green),
463 was reversed by INK treatment (Fig. 6B, LY group, red vs blue). Second, INK reduced the number
464 of AL in TRGL/Q175-Veh compared to TRGL-Veh (Fig. 6B, AL group, red vs blue), implying
465 improved AL clearance and likely providing the basis for restoration of normal LY number.
466 Together, the data suggest that autophagy phenotype in 7-mo Q175 is measurable but milder than
467 that in the 17-mo-old mice shown in Fig. 3A and that INK has the potential to modulate the
468 autophagy pathway and restore normal function at this mild disease stage.
469
470 **mTOR inhibition mitigates mHTT-related aggresome pathology**
471 Importantly, we found that HD-like pathology such as mHTT IBs and associated protein
472 aggregation of adaptor proteins, p62 and Ub, was ameliorated by INK treatment. Confocal images
473 demonstrated that mHTT positive particles/inclusions were substantially reduced in INK-treated
474 7-mo-old TRGL/Q175, compared to Veh-treated TRGL/Q175 mice (Fig. 7A). Moreover, p62-IR
475 or Ub-IR also changed in a similar trend (Fig. 7A), consistent with the high degree of colocalization
476 of mHTT/p62/Ub signals shown in Fig. 2A. The corresponding quantitative analysis, shown as
477 Area Covered by either mHTT-, p62- or Ub-IR on a per cell basis, confirmed statistically
478 significant decreases in the Total Area Covered by mHTT-, p62-signals (Fig. 7B1). With the
479 assistance of the endogenous tfLC3 signal (particularly the mRFP signal) in the TRGL to identify
480 the association status of the mHTT-, p62- or Ub-IR with AVs, the images were additionally
481 quantified to generate the separated "Area Covered by the AV-associated Form" (Fig. 7B2) and
482 "Area Covered by the AV-unassociated Form" (Fig. 7B3) of mHTT-, p62- or Ub- signals. The

483 results collectively suggest decreased mHTT-, p62- or Ub-IR in treated compared to untreated
484 TRGL/Q175, implying that INK treatment was able to promote the clearance of mHTT and related
485 receptor proteins p62 and/or Ub.
486
487 **mTOR inhibition does not reverse preexisting DARPP-32-IR reduction in TRGL/Q175**
488 Finally, we evaluated neurodegenerative changes by employing DARPP-32 IHC on brain
489 sections of Veh-treated or INK-treated TRGL/Q175. Similar to what was found in 17-mo-old mice
490 (Fig. 4), the group of TRGL/Q175-Veh, even at this young age (7-mo), already exhibited a
491 diminished DARPP-32-IR signal compared to that in TRGL-Veh (Fig. 8A, B). However, no
492 differences between the untreated and INK-treated TRGL/Q175 groups were established by
493 quantitative analysis (Fig. 8A, B). Thus, the result suggests a lack of effectiveness of INK in
494 reversing this pre-existing phonotype, implying that earlier intervention may be necessary [41].
495
496
497 **DISCUSSION**
498 Previous studies in cell and animal models have documented roles of HTT and mHTT in
499 autophagy in relation to HD [for reviews, see 15, 31, 43]. WT HTT participates in normal
500 autophagy by releasing ULK1 via mTOR inhibition and serving as a scaffold to facilitate cargo
501 sequestration by enhancing p62 interaction with LC3 and ubiquitinated cargos [50, 61]. mHTT in
502 HD may activate autophagy by sequestering and thus inhibiting mTOR [57]. Most mHTT effects
503 in cellular and mouse HD models appear to be inhibitory for autophagy induction steps, from
504 initiation signaling and phagophore nucleation to cargo recognition/AP formation [3, 44, 56, 61,
505 74]. In addition, mHTT may disturb endolysosomal homeostasis by reducing exocytosis and
506 promoting AL accumulation [78]. In the current study using Q175, we have found that mHTT is
507 an ALP substrate and that the ALP is relatively intact, with some late-onset minor alterations, such
508 as insufficient mTOR activity reflected by lowered phospho-p70S6K level and ratio of phospho-
509 ULK1 (S757)/total ULK1, lysosome depletion and AL/pa-AL elevation. This mild late-onset
510 nature of ALP pathogenesis allowed us to modulate ALP with a mTOR inhibitor in 6-mo-old
511 TRGL/Q175 which resulted in positive effects on rescuing Q175 phenotypes including
512 normalization of AL/LY subtypes and reduction in aggresome pathology.
513

514 **ALP impairments in Q175 are mild and late-onset**

515 In the current study, we assessed ALP alterations in the Q175 model by analyzing protein
516 markers in all phases of the ALP including autophagy induction signaling, membrane
517 nucleation/AP formation, autophagy adaptor proteins and AL formation/substrate degradation. By
518 immunoblot analysis, alterations in the tested marker proteins even at 17 months of age in
519 TRGL/Q175 mice were limited to a reduction in p-P70S6K (T389), similar to that reported
520 previously [57], and a reduced ratio of p-ULK1 (S757)/total ULK1 as a result of increased total
521 ULK1. While these two alterations together would suggest a lower mTOR activity and autophagy
522 activation, consequential alterations of downstream markers, particularly proteins in the ATG14-
523 containing Beclin-1/VPS34 complex, were not detected. Although 4 out of the 10 tested
524 TRGL/Q175 mice exhibited very low levels of p-ATG14, implying a deficit in this complex as
525 previously reported [74], variation among animals was too great to draw statistical conclusions.
526 In this regard, mice used in the current study were heterozygous, which results in less autophagy
527 alteration than that reported in homozygous mice using certain autophagy markers [1]. It may also
528 be noted in our experience that immunoblot analysis of brain tissue averages contributions from
529 varied cell types that may respond to disease states in opposite directions and mask changes in a
530 given cell population. Thus, we also applied a neuron-specific analysis using our neuron-specific
531 tfLC3 reporter and hue-angle based image quantification approach, which yielded more sensitive
532 detection and findings.

533 In brain sections from 17-mo-old TRGL/Q175 mice, we observed increased numbers of AL
534 including the population of pa-AL and reduced numbers of LY. Such changes in AL/pa-AL were
535 not readily observed in TRGL/Q175 mice at 2 months (not shown) or 7 months (e.g., Fig. 6B,
536 which only exhibited a reduction in LY number) of age, indicating that even if these alterations
537 signify an existence of impairments in the late phase of the ALP, they do not occur until a later
538 age (e.g., 17 mo). Importantly, this pattern of late-onset ALP pathology progression, e.g., AL/pa-
539 AL increases, is consistent with our findings from HD human brains [9] where enlarged CTSD-
540 positive AL accumulate and cluster in affected neuronal populations at the late disease stages (HD3
541 and HD4). These findings suggest that the overall autophagy function in heterozygous Q175 is
542 largely maintained until the relatively late disease stage and provide a rationale to stimulate
543 autophagy as a therapeutic intervention when the autophagy machinery is still functional, which

544 would generate beneficial effects. We obtained support for this concept in the subsequent study
545 with mTORi INK when administered to TRGL/Q175 at 6 months of age for three weeks.
546
547 **Autophagy as a primary mechanism for INK-enhanced clearance of small mHTT species**
548 One of the key findings from this study is the reduction of mHTT-IR in neurons detected by
549 immunolabeling after the 3-week oral treatment with mTORi INK (Fig. 7). This beneficial
550 outcome from the drug treatment is interpreted as a primary result of the manipulation/stimulation
551 of autophagy by the compound, leading to enhanced autophagy clearance of mHTT species
552 including smaller, presumably soluble, species and larger aggregates such as the IBs. This
553 interpretation is supported by the following considerations and evidence. First, in theory, the
554 compound used for the treatment is a mTORi so is expected to enhance autophagy [8, 29]. Second,
555 target engagement is achieved as clearly reflected by the diminished levels of mTOR-mediated
556 phosphorylation on mTOR itself (S2481), ULK1 (S757) and p-S6 (S240/S244), along with
557 changes in proteins downstream of mTOR, such as p-ATG14 (S29) and LC3. Third, hue-angle
558 based confocal image analysis of AL/LY subtypes reveals a reduced AL number and an increased
559 LY number in INK-treated TRGL/Q175 compared to Veh-treated TRGL/Q175. The findings from
560 this analysis of AL/LY subtypes highlights the advantages of crossing TRGL with Q175 mice to
561 evaluate autophagy modulators on the ALP, consistent with a notion of developing better tools
562 capable of investigating autophagy flux *in vivo* [48, 71].
563 Our confocal microscopy analyses revealed mHTT signal in CTSD-positive vesicles, which
564 can be classified as AL based on their LC3 fluorescence, and IEM detected mHTT-silver-enhanced
565 gold particles in AP and AL including lipofuscin granules. Both findings indicate the existence of
566 mHTT species inside the ALP as autophagy substrates. The presence of low levels of mHTT in
567 CTSD-positive AL also implies a constitutive functional degradation event of mHTT in AL (Fig.
568 2B1, 10-mo-old mouse). This is in contrast to the case in young AD mouse models where early-
569 onset autophagy-stress exhibited severe substrate accumulation (e.g., reflected by strong LC3
570 signal) due to deficits of degradative functions within AL. [36]. A reduced level in the portion of
571 AV-associated mHTT signals (Fig. 7B2) by mTORi INK further suggests that mHTT degradation
572 has been enhanced after manipulating the ALP. This AV-associated mHTT pool is considered to
573 be corresponding to the mHTT-silver-enhanced gold signal under IEM (Fig. 2B2), i.e., amorphous
574 and existing within the lumen of AV. Such mHTT localization and ultrastructural features are

575 consistent with recent findings that mHTT proteins exogenously added to Q175 brain sections for
576 incubation are recruited to multivesicular bodies/amphisomes, AL and residual bodies (lipofuscin
577 granules), and ultrastructurally localized to non-fibrillar, electron-lucent regions within the lumen
578 of these organelles [78].
579
580 **Possible autophagy-related mechanism for the clearance of large mHTT IBs**
581 It is notable that the AV-non-associated form of mHTT (i.e., did not show colocalization
582 with the endogenous tfLC3 signal implying that they might not have a contact with AVs) decrease
583 more obviously after drug-treatment, along with the reductions in p62 and Ub signals (Fig. 7B3).
584 These mHTT species are mainly larger aggresomes/IBs, including those within the nuclei. Based
585 on our mHTT-IEM observation (Fig. 1B), the IBs in Q175 brain are fibrillar aggregates in the
586 nucleus and cytoplasm, exhibiting a homogeneous feature in shape (i.e., round/oval cotton-ball)
587 and in content (i.e., short fine fibrils), similar to the nuclear IBs we found in human HD brains [9],
588 whose cytoplasmic and neuritic IBs, however, also exhibit more heterogeneous compositions such
589 as a mixture of fine fibrils with AVs, fingerprint-like structures or bundles of microtubules. In the
590 current study, we did not observe that a whole IB is contained within an AP or AL in our EM
591 examination, raising a question of how these larger aggregates could be degraded by the autophagy
592 machinery after an autophagy activation by mTOR inhibition. This issue is informed by findings
593 that the mHTT species are dynamic and the aggregates can form as different phases (liquid-like or
594 solid-like), making it possible for mHTT species to move out or into IBs [2, 40, 54, 58] and to
595 shuttle between the nucleus and the cytoplasm [4, 75]. Thus, it is speculated that under the
596 autophagy activated condition induced by mTOR inhibition, the enhanced clearance of mHTT in
597 the ALP pool would promote movements of mHTT species from the IB forms, leading to a
598 reduction on the overall mHTT load.
599
600 **UPS as an additional mechanism for the clearance of mHTT species**
601 Even if INK is a mTORi mainly targeting autophagy, we cannot completely exclude
602 additional contributions from the UPS for the observed reduction of mHTT species given the
603 crosstalk between the two proteolytic systems. It is well accepted that autophagy plays a more
604 important role in the clearance of larger protein aggregates such as aggresomes/IBs [63]. For
605 example, autophagy is involved in the degradation of p62 bodies [10] and autophagy markers are

606 colocalized with cytoplasmic mHTT IBs [23]. However, there is also evidence for degradation of
607 polyQ aggregates in the nuclei [24], which contain p62 condensates as a hub for UPS-mediated
608 nuclear protein turnover [19]. We observed a high level of colocalization of mHTT with p62 and
609 Ub in aggregates at both intranuclear and extranuclear locations (Fig. 2A), which is presumably
610 more related to the UPS hub and autophagy, respectively. It is possible that stimulation of
611 autophagy is reducing the mHTT in the cytoplasm and thereby partially relieves the burden of the
612 proteasome both in the cytoplasm and in the nucleus so that the nuclear proteasome operates more
613 effectively.
614
615 In summary, Q175 models, as detected in the current study, develop ALP alterations late in
616 the disease progression. Although milder than what is seen in late-stage HD human brain [9], there
617 are similarities in ALP pathobiology between human HD brains and Q175 brains. These include
618 late-onset nature, mHTT as an ALP substrate, increased AL/pa-AL, mouse IB ultrastructural
619 feature similar to the common fine fibril type of human IBs. The late-onset mild ALP pathology
620 in Q175 is different from the severe AV accumulation in mouse models of AD as mentioned above
621 [36]. Together, the mild and late-onset nature of ALP alterations in Q175 provides a basis for
622 manipulating autophagy to be a promising therapeutic strategy if the manipulations (e.g.,
623 stimulating autophagy with mTORi as in this study) are applied when the autophagy machinery is
624 largely undamaged. This has been validated to be successful in this study as demonstrated by the
625 INK-induced reduction of mHTT species along with other beneficial effects, consistent with
626 findings from similar studies and supporting the general notion of lowering mHTT as a therapeutic
627 strategy for HD [6, 14].
628

629 **DECLARATIONS:**

630 **ACKNOWLEDGMENTS**

631 We are grateful to Dr. T Yoshimori (Osaka University, Japan) for the mRFP-eEGFP-LC3 construct
632 used in the TRGL mice.

633

634 **Funding**

635 This work was supported by the CHDI Foundation (R.A.N.) and the National Institute of Aging
636 (P01 AG017617 to R.A.N.).

637

638 **Author Contributions**

639 Conceptualization and design: RAN, DSY, DMM; Investigation, data collection and analysis: PS,
640 DSY, CNG, JP, CH, VK; Writing - original draft preparation: DSY; Writing - review and editing:
641 DSY, RAN, DMM, PS, CNG, MR; Funding acquisition: RAN; Supervision: DSY, RAN.

642

643 **Competing Interest**

644 All authors declare no conflict of interests.

645

646 **Ethics Approval**

647 The animal procedures conducted in this study were approved by the Institutional Animal Care
648 and Use Committee at the NKI.

649

650

651 References

652

653 1 Abd-Elrahman KS, Hamilton A, Hutchinson SR, Liu F, Russell RC, Ferguson SSG (2017)
654 mGluR5 antagonism increases autophagy and prevents disease progression in the zQ175
655 mouse model of Huntington's disease. Sci Signal 10: Doi 10.1126/scisignal.aan6387

656 2 Aktar F, Burudpakdee C, Polanco M, Pei S, Swayne TC, Lipke PN et al (2019) The
657 huntingtin inclusion is a dynamic phase-separated compartment. Life Sci Alliance 2: Doi
658 10.26508/lsa.201900489

659 3 Ashkenazi A, Bento CF, Ricketts T, Vicinanza M, Siddiqi F, Pavel M et al (2017)
660 Polyglutamine tracts regulate beclin 1-dependent autophagy. Nature 545: 108-111. Doi
661 10.1038/nature22078

662 4 Atwal RS, Xia J, Pinchev D, Taylor J, Epand RM, Truant R (2007) Huntingtin has a
663 membrane association signal that can modulate huntingtin aggregation, nuclear entry and
664 toxicity. Human molecular genetics 16: 2600-2615. Doi 10.1093/hmg/ddm217

665 5 Baiamonte BA, Lee FA, Brewer ST, Spano D, LaHoste GJ (2013) Attenuation of Rhes
666 activity significantly delays the appearance of behavioral symptoms in a mouse model of
667 Huntington's disease. PLoS One 8: e53606. Doi 10.1371/journal.pone.0053606

668 6 Barker RA, Fujimaki M, Rogers P, Rubinsztein DC (2020) Huntingtin-lowering strategies
669 for Huntington's disease. Expert opinion on investigational drugs 29: 1125-1132. Doi
670 10.1080/13543784.2020.1804552

671 7 Bates GP, Dorsey R, Gusella JF, Hayden MR, Kay C, Leavitt BR et al (2015) Huntington
672 disease. Nat Rev Dis Primers 1: 15005. Doi 10.1038/nrdp.2015.5

673 8 Bensalem J, Fourrier C, Hein LK, Hassiotis S, Proud CG, Sargeant TJ (2021) Inhibiting
674 mTOR activity using AZD2014 increases autophagy in the mouse cerebral cortex.
675 Neuropharmacology 190: 108541. Doi 10.1016/j.neuropharm.2021.108541

676 9 Berg MJ, Veeranna, Rosa CM, Kumar A, Mohan PS, Stavrides P et al (2024) Pathobiology
677 of the autophagy-lysosomal pathway in the Huntington's disease brain. bioRxiv:
678 2024.2005.2029.596470. Doi https://doi.org/10.1101/2024.05.29.596470

679 10 Bjørkøy G, Lamark T, Brech A, Outzen H, Perander M, Øvervatn A et al (2005)
680 p62/SQSTM1 forms protein aggregates degraded by autophagy and has a protective effect

681 on huntingtin-induced cell death. J Cell Biol 171: 603-614. Doi
682 https://doi.org/10.1083/jcb.200507002
683 11 Boland B, Yu WH, Corti O, Mollereau B, Henriques A, Bezard E et al (2018) Promoting
684 the clearance of neurotoxic proteins in neurodegenerative disorders of ageing. Nature
685 reviews Drug discovery 17: 660-688. Doi 10.1038/nrd.2018.109
686 12 Carty N, Berson N, Tillack K, Thiede C, Scholz D, Kottig K et al (2015) Characterization
687 of HTT inclusion size, location, and timing in the zQ175 mouse model of Huntington's
688 disease: an in vivo high-content imaging study. PLoS One 10: e0123527. Doi
689 10.1371/journal.pone.0123527
690 13 Cataldo AM, Thayer CY, Bird ED, Wheelock TR, Nixon RA (1990) Lysosomal proteinase
691 antigens are prominently localized within senile plaques of Alzheimer's disease: evidence
692 for a neuronal origin. Brain Res 513: 181-192.
693 14 Cortes CJ, La Spada AR (2014) The many faces of autophagy dysfunction in Huntington's
694 disease: from mechanism to therapy. Drug discovery today 19: 963-971. Doi
695 10.1016/j.drudis.2014.02.014
696 15 Croce KR, Yamamoto A (2019) A role for autophagy in Huntington's disease. Neurobiol
697 Dis 122: 16-22. Doi 10.1016/j.nbd.2018.08.010
698 16 Deng Y, Wang H, Joni M, Sekhri R, Reiner A (2021) Progression of basal ganglia
699 pathology in heterozygous Q175 knock-in Huntington's disease mice. J Comp Neurol 529:
700 1327-1371. Doi 10.1002/cne.25023
701 17 DiFiglia M, Sapp E, Chase KO, Davies SW, Bates GP, Vonsattel JP et al (1997)
702 Aggregation of huntingtin in neuronal intranuclear inclusions and dystrophic neurites in
703 brain. Science 277: 1990-1993.
704 18 Franklin GL, Teive HAG, Tensini FS, Camargo CHF, de Lima NSC, de Dos Santos DC et
705 al (2024) The Huntington's Disease Gene Discovery. Mov Disord 39: 227-234. Doi
706 10.1002/mds.29703
707 19 Fu A, Cohen-Kaplan V, Avni N, Livneh I, Ciechanover A (2021) p62-containing,
708 proteolytically active nuclear condensates, increase the efficiency of the ubiquitin-
709 proteasome system. Proc Natl Acad Sci U S A 118: Doi 10.1073/pnas.2107321118

710 20 Gutekunst CA, Li SH, Yi H, Mulroy JS, Kuemmerle S, Jones R et al (1999) Nuclear and
711 neuropil aggregates in Huntington's disease: relationship to neuropathology. J Neurosci 19:
712 2522-2534. Doi https://doi.org/10.1523/jneurosci.19-07-02522.1999
713 21 Heikkinen T, Bragge T, Kuosmanen J, Parkkari T, Gustafsson S, Kwan M et al (2021)
714 Global Rhes knockout in the Q175 Huntington's disease mouse model. PLoS One 16:
715 e0258486. Doi 10.1371/journal.pone.0258486
716 22 Hickey MA, Kosmalska A, Enayati J, Cohen R, Zeitlin S, Levine MS et al (2008) Extensive
717 early motor and non-motor behavioral deficits are followed by striatal neuronal loss in
718 knock-in Huntington's disease mice. Neuroscience 157: 280-295. Doi
719 10.1016/j.neuroscience.2008.08.041
720 23 Iwata A, Christianson JC, Bucci M, Ellerby LM, Nukina N, Forno LS et al (2005) Increased
721 susceptibility of cytoplasmic over nuclear polyglutamine aggregates to autophagic
722 degradation. Proc Natl Acad Sci U S A 102: 13135-13140. Doi 10.1073/pnas.0505801102
723 24 Iwata A, Nagashima Y, Matsumoto L, Suzuki T, Yamanaka T, Date H et al (2009)
724 Intranuclear degradation of polyglutamine aggregates by the ubiquitin-proteasome system.
725 J Biol Chem 284: 9796-9803. Doi 10.1074/jbc.M809739200
726 25 Jamilloux Y, Lagrange B, Di Micco A, Bourdonnay E, Provost A, Tallant R et al (2018) A
727 proximity-dependent biotinylation (BioID) approach flags the p62/sequestosome-1 protein
728 as a caspase-1 substrate. J Biol Chem 293: 12563-12575. Doi 10.1074/jbc.RA117.000435
729 26 Jiang A, Handley RR, Lehnert K, Snell RG (2023) From Pathogenesis to Therapeutics: A
730 Review of 150 Years of Huntington's Disease Research. International journal of molecular
731 sciences 24: Doi 10.3390/ijms241613021
732 27 Jiang Y, Alam JJ, Gomperts SN, Maruff P, Lemstra AW, Germann UA et al (2022)
733 Preclinical and randomized clinical evaluation of the p38alpha kinase inhibitor
734 neflamapimod for basal forebrain cholinergic degeneration. Nature communications 13:
735 5308. Doi 10.1038/s41467-022-32944-3
736 28 Kim A, Lalonde K, Truesdell A, Gomes Welter P, Brocardo PS, Rosenstock TR et al (2021)
737 New Avenues for the Treatment of Huntington's Disease. International journal of
738 molecular sciences 22: Doi 10.3390/ijms22168363
739 29 Kim YC, Guan KL (2015) mTOR: a pharmacologic target for autophagy regulation. J Clin
740 Invest 125: 25-32. Doi 10.1172/JCI73939

741 30 Kim YJ, Yi Y, Sapp E, Wang Y, Cuiffo B, Kegel KB et al (2001) Caspase 3-cleaved N-
742 terminal fragments of wild-type and mutant huntingtin are present in normal and
743 Huntington's disease brains, associate with membranes, and undergo calpain-dependent
744 proteolysis. Proc Natl Acad Sci U S A 98: 12784-12789. Doi 10.1073/pnas.221451398
745 31 Klionsky DJ, Petroni G, Amaravadi RK, Baehrecke EH, Ballabio A, Boya P et al (2021)
746 Autophagy in major human diseases. EMBO J 40: e108863. Doi
747 10.15252/embj.2021108863
748 32 Ko J, Isas JM, Sabbaugh A, Yoo JH, Pandey NK, Chongtham A et al (2018) Identification
749 of distinct conformations associated with monomers and fibril assemblies of mutant
750 huntingtin. Human molecular genetics 27: 2330-2343. Doi 10.1093/hmg/ddy141
751 33 Kolla R, Gopinath P, Ricci J, Reif A, Rostami I, Lashuel HA (2021) A New
752 Chemoenzymatic Semisynthetic Approach Provides Insight into the Role of
753 Phosphorylation beyond Exon1 of Huntingtin and Reveals N-Terminal Fragment Length-
754 Dependent Distinct Mechanisms of Aggregation. Journal of the American Chemical
755 Society 143: 9798-9812. Doi 10.1021/jacs.1c03108
756 34 Lee JH, Rao MV, Yang DS, Stavrides P, Im E, Pensalfini A et al (2019) Transgenic
757 expression of a ratiometric autophagy probe specifically in neurons enables the
758 interrogation of brain autophagy in vivo. Autophagy 15: 543-557. Doi
759 10.1080/15548627.2018.1528812
760 35 Lee JH, Tecedor L, Chen YH, Monteys AM, Sowada MJ, Thompson LM et al (2015)
761 Reinstating aberrant mTORC1 activity in Huntington's disease mice improves disease
762 phenotypes. Neuron 85: 303-315. Doi 10.1016/j.neuron.2014.12.019
763 36 Lee JH, Yang DS, Goulbourne CN, Im E, Stavrides P, Pensalfini A et al (2022) Faulty
764 autolysosome acidification in Alzheimer's disease mouse models induces autophagic build-
765 up of Abeta in neurons, yielding senile plaques. Nat Neurosci 25: 688-701. Doi
766 10.1038/s41593-022-01084-8
767 37 Li H, Li SH, Cheng AL, Mangiarini L, Bates GP, Li XJ (1999) Ultrastructural localization
768 and progressive formation of neuropil aggregates in Huntington's disease transgenic mice.
769 Human molecular genetics 8: 1227-1236. Doi 10.1093/hmg/8.7.1227

770 38 Lie PPY, Yang DS, Stavrides P, Goulbourne CN, Zheng P, Mohan PS et al (2021) Post-
771 Golgi carriers, not lysosomes, confer lysosomal properties to pre-degradative organelles in
772 normal and dystrophic axons. Cell Rep 35: 109034. Doi 10.1016/j.celrep.2021.109034
773 39 Lie PPY, Yoo L, Goulbourne CN, Berg MJ, Stavrides P, Huo C et al (2022) Axonal
774 transport of late endosomes and amphisomes is selectively modulated by local Ca(2+)
775 efflux and disrupted by PSEN1 loss of function. Sci Adv 8: eabj5716. Doi
776 10.1126/sciadv.abj5716
777 40 Liu KY, Shyu YC, Barbaro BA, Lin YT, Chern Y, Thompson LM et al (2015) Disruption
778 of the nuclear membrane by perinuclear inclusions of mutant huntingtin causes cell-cycle
779 re-entry and striatal cell death in mouse and cell models of Huntington's disease. Human
780 molecular genetics 24: 1602-1616. Doi 10.1093/hmg/ddu574
781 41 Marchionini DM, Liu JP, Ambesi-Impiombato A, Kerker K, Cirillo K, Bansal M et al
782 (2022) Benefits of global mutant huntingtin lowering diminish over time in a Huntington's
783 disease mouse model. JCI insight 7: Doi 10.1172/jci.insight.161769
784 42 Mario Isas J, Pandey NK, Xu H, Teranishi K, Okada AK, Fultz EK et al (2021) Huntingtin
785 fibrils with different toxicity, structure, and seeding potential can be interconverted. Nature
786 communications 12: 4272. Doi 10.1038/s41467-021-24411-2
787 43 Martin DD, Ladha S, Ehrnhoefer DE, Hayden MR (2015) Autophagy in Huntington
788 disease and huntingtin in autophagy. Trends Neurosci 38: 26-35. Doi
789 10.1016/j.tins.2014.09.003
790 44 Martinez-Vicente M, Talloczy Z, Wong E, Tang G, Koga H, Kaushik S et al (2010) Cargo
791 recognition failure is responsible for inefficient autophagy in Huntington's disease. Nat
792 Neurosci 13: 567-576. Doi https://doi.org/10.1038/nn.2528
793 45 Menalled LB, Kudwa AE, Miller S, Fitzpatrick J, Watson-Johnson J, Keating N et al (2012)
794 Comprehensive behavioral and molecular characterization of a new knock-in mouse model
795 of Huntington's disease: zQ175. PLoS One 7: e49838. Doi 10.1371/journal.pone.0049838
796 46 Menalled LB, Sison JD, Dragatsis I, Zeitlin S, Chesselet MF (2003) Time course of early
797 motor and neuropathological anomalies in a knock-in mouse model of Huntington's disease
798 with 140 CAG repeats. J Comp Neurol 465: 11-26. Doi 10.1002/cne.10776
799 47 Mende-Mueller LM, Toneff T, Hwang SR, Chesselet MF, Hook VY (2001) Tissue-specific
800 proteolysis of Huntingtin (htt) in human brain: evidence of enhanced levels of N- and C-

801 terminal htt fragments in Huntington's disease striatum. J Neurosci 21: 1830-1837. Doi
802 https://doi.org/10.1523/jneurosci.21-06-01830.2001
803 48 Nixon RA (2013) The role of autophagy in neurodegenerative disease. Nat Med 19: 983-
804 997. Doi https://doi.org/10.1038/nm.3232
805 49 Norman JM, Cohen GM, Bampton ET (2010) The in vitro cleavage of the hAtg proteins
806 by cell death proteases. Autophagy 6: 1042-1056. Doi 10.4161/auto.6.8.13337
807 50 Ochaba J, Lukacsovich T, Csikos G, Zheng S, Margulis J, Salazar L et al (2014) Potential
808 function for the Huntingtin protein as a scaffold for selective autophagy. Proc Natl Acad
809 Sci U S A 111: 16889-16894. Doi 10.1073/pnas.1420103111
810 51 Ouimet CC, Langley-Gullion KC, Greengard P (1998) Quantitative immunocytochemistry
811 of DARPP-32-expressing neurons in the rat caudatoputamen. Brain Res 808: 8-12. Doi
812 10.1016/s0006-8993(98)00724-0
813 52 Park JM, Jung CH, Seo M, Otto NM, Grunwald D, Kim KH et al (2016) The ULK1
814 complex mediates MTORC1 signaling to the autophagy initiation machinery via binding
815 and phosphorylating ATG14. Autophagy 12: 547-564. Doi
816 10.1080/15548627.2016.1140293
817 53 Peng Q, Wu B, Jiang M, Jin J, Hou Z, Zheng J et al (2016) Characterization of Behavioral,
818 Neuropathological, Brain Metabolic and Key Molecular Changes in zQ175 Knock-In
819 Mouse Model of Huntington's Disease. PLoS One 11: e0148839. Doi
820 10.1371/journal.pone.0148839
821 54 Peskett TR, Rau F, O'Driscoll J, Patani R, Lowe AR, Saibil HR (2018) A Liquid to Solid
822 Phase Transition Underlying Pathological Huntingtin Exon1 Aggregation. Molecular cell
823 70: 588-601.e586. Doi 10.1016/j.molcel.2018.04.007
824 55 Pressl C, Mätlik K, Kus L, Darnell P, Luo JD, Paul MR et al (2024) Selective vulnerability
825 of layer 5a corticostriatal neurons in Huntington's disease. Neuron: Doi
826 10.1016/j.neuron.2023.12.009
827 56 Pryor WM, Biagioli M, Shahani N, Swarnkar S, Huang WC, Page DT et al (2014)
828 Huntingtin promotes mTORC1 signaling in the pathogenesis of Huntington's disease. Sci
829 Signal 7: ra103. Doi 10.1126/scisignal.2005633

830 57 Ravikumar B, Vacher C, Berger Z, Davies JE, Luo S, Oroz LG et al (2004) Inhibition of
831 mTOR induces autophagy and reduces toxicity of polyglutamine expansions in fly and
832 mouse models of Huntington disease. Nat Genet 36: 585-595. Doi 10.1038/ng1362
833 58 Riguet N, Mahul-Mellier AL, Maharjan N, Burtscher J, Croisier M, Knott G et al (2021)
834 Nuclear and cytoplasmic huntingtin inclusions exhibit distinct biochemical composition,
835 interactome and ultrastructural properties. Nature communications 12: 6579. Doi
836 10.1038/s41467-021-26684-z
837 59 Rose C, Menzies FM, Renna M, Acevedo-Arozena A, Corrochano S, Sadiq O et al (2010)
838 Rilmenidine attenuates toxicity of polyglutamine expansions in a mouse model of
839 Huntington's disease. Human molecular genetics 19: 2144-2153. Doi 10.1093/hmg/ddq093
840 60 Rothe T, Deliano M, Wojtowicz AM, Dvorzhak A, Harnack D, Paul S et al (2015)
841 Pathological gamma oscillations, impaired dopamine release, synapse loss and reduced
842 dynamic range of unitary glutamatergic synaptic transmission in the striatum of
843 hypokinetic Q175 Huntington mice. Neuroscience 311: 519-538. Doi
844 10.1016/j.neuroscience.2015.10.039
845 61 Rui YN, Xu Z, Patel B, Chen Z, Chen D, Tito A et al (2015) Huntingtin functions as a
846 scaffold for selective macroautophagy. Nat Cell Biol 17: 262-275. Doi 10.1038/ncb3101
847 62 Sanchez-Garrido J, Sancho-Shimizu V, Shenoy AR (2018) Regulated proteolysis of
848 p62/SQSTM1 enables differential control of autophagy and nutrient sensing. Sci Signal
849 11: Doi 10.1126/scisignal.aat6903
850 63 Sarkar S, Rubinsztein DC (2008) Huntington's disease: degradation of mutant huntingtin
851 by autophagy. The FEBS journal 275: 4263-4270. Doi 10.1111/j.1742-4658.2008.06562.x
852 64 Sarkar S, Rubinsztein DC (2008) Small molecule enhancers of autophagy for
853 neurodegenerative diseases. Molecular bioSystems 4: 895-901. Doi 10.1039/b804606a
854 65 Schmidt SD, Nixon RA, Mathews PM (2012) Tissue processing prior to analysis of
855 Alzheimer's disease associated proteins and metabolites, including Abeta. Methods in
856 molecular biology (Clifton, NJ) 849: 493-506. Doi 10.1007/978-1-61779-551-0_33
857 66 Sotrel A, Paskevich PA, Kiely DK, Bird ED, Williams RS, Myers RH (1991)
858 Morphometric analysis of the prefrontal cortex in Huntington's disease. Neurology 41:
859 1117-1123.

860 67 Tanaka M, Machida Y, Niu S, Ikeda T, Jana NR, Doi H et al (2004) Trehalose alleviates
861 polyglutamine-mediated pathology in a mouse model of Huntington disease. Nat Med 10:
862 148-154. Doi 10.1038/nm985
863 68 The-Huntington's-Disease-Collaborative-Research-Group (1993) A novel gene containing
864 a trinucleotide repeat that is expanded and unstable on Huntington's disease chromosomes.
865 . Cell 72: 971-983. Doi 10.1016/0092-8674(93)90585-e
866 69 Trottier Y, Lutz Y, Stevanin G, Imbert G, Devys D, Cancel G et al (1995) Polyglutamine
867 expansion as a pathological epitope in Huntington's disease and four dominant cerebellar
868 ataxias. Nature 378: 403-406. Doi 10.1038/378403a0
869 70 Valionyte E, Yang Y, Griffiths SA, Bone AT, Barrow ER, Sharma V et al (2022) The
870 caspase-6-p62 axis modulates p62 droplets based autophagy in a dominant-negative
871 manner. Cell death and differentiation 29: 1211-1227. Doi 10.1038/s41418-021-00912-x
872 71 Vodicka P, Lim J, Williams DT, Kegel KB, Chase K, Park H et al (2014) Assessment of
873 chloroquine treatment for modulating autophagy flux in brain of WT and HD mice. Journal
874 of Huntington's disease 3: 159-174. Doi 10.3233/jhd-130081
875 72 Vonsattel JP (2008) Huntington disease models and human neuropathology: similarities
876 and differences. Acta Neuropathol 115: 55-69. Doi 10.1007/s00401-007-0306-6
877 73 Vonsattel JP, Myers RH, Stevens TJ, Ferrante RJ, Bird ED, Richardson EP, Jr. (1985)
878 Neuropathological classification of Huntington's disease. J Neuropathol Exp Neurol 44:
879 559-577. Doi 10.1097/00005072-198511000-00003
880 74 Wold MS, Lim J, Lachance V, Deng Z, Yue Z (2016) ULK1-mediated phosphorylation of
881 ATG14 promotes autophagy and is impaired in Huntington's disease models. Molecular
882 neurodegeneration 11: 76. Doi 10.1186/s13024-016-0141-0
883 75 Xia J, Lee DH, Taylor J, Vandelft M, Truant R (2003) Huntingtin contains a highly
884 conserved nuclear export signal. Human molecular genetics 12: 1393-1403. Doi
885 10.1093/hmg/ddg156
886 76 Yang DS, Lee JH, Nixon RA (2009) Monitoring autophagy in Alzheimer's disease and
887 related neurodegenerative diseases. Methods Enzymol 453: 111-144. Doi 10.1016/S0076-
888 6879(08)04006-8

889 77 Yang J, Zhang C (2023) Targeting the autophagy-lysosomal pathway in Huntington
890 disease: a pharmacological perspective. Frontiers in aging neuroscience 15: 1175598. Doi
891 10.3389/fnagi.2023.1175598
892 78 Zhou Y, Peskett TR, Landles C, Warner JB, Sathasivam K, Smith EJ et al (2021)
893 Correlative light and electron microscopy suggests that mutant huntingtin dysregulates the
894 endolysosomal pathway in presymptomatic Huntington's disease. Acta neuropathologica
895 communications 9: 70. Doi 10.1186/s40478-021-01172-z
896

Fig. 1. Identification of inclusions and HTT molecular species in Q175 mice.

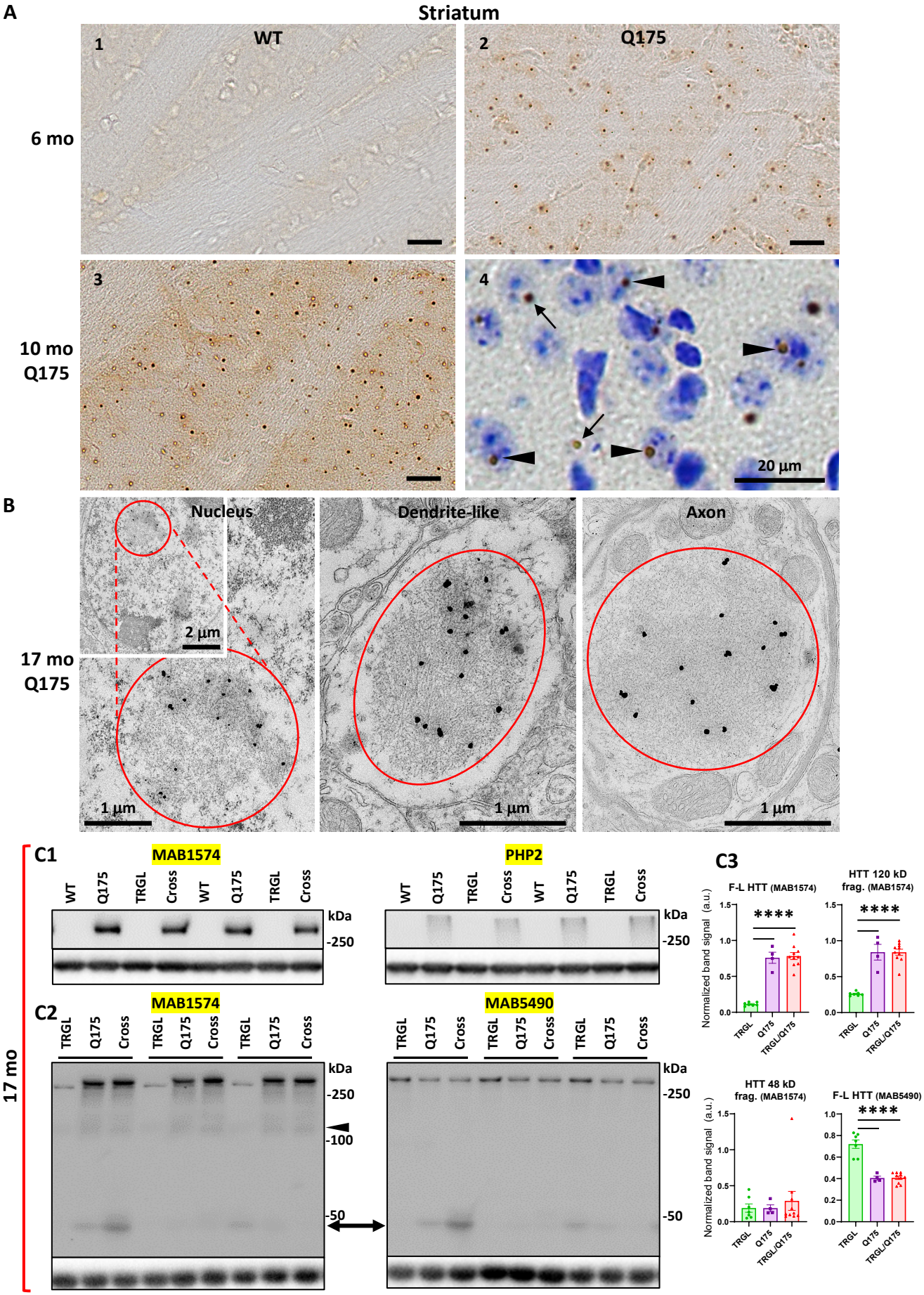

Fig. 1 Identification of inclusions and HTT molecular species in Q175 mice.

(A) IHC detects age-dependent increase in the number of mHTT inclusions. Brain sections from 6-mo- and 10-mo-old WT and Q175 mice were processed for IHC with antibody mEM48 (MAB5374) directed against mHTT (A). Images from sections without (A1-3) or with (A4) a cresyl violet counterstain are shown where the dark-brown puncta represent mHTT-positive inclusions. Arrowheads depict neuronal intranuclear inclusions (NIIs), determined with the assistance from the nuclear labeling by cresyl violet, while arrows indicate extranuclear inclusions, primarily the neuritic inclusion in the neuropil. Bars = 20 μm.

(B) mHTT inclusions are detected in nucleus, dendrites and axons of Q175 brains by IEM. Sagittal vibratome brain sections of 17-mo-old Q175 were cut and went through EM processing. Small blocks were obtained from the striatal areas for ultrathin sectioning. Tissue containing grids were processed for immunogold labeling procedure with antibody mEM48, using 10 nm gold followed by silver enhancement. Structures showing high level of silver-enhanced gold labeling were considered as mHTT-positive.

(C) Various forms of HTT molecules are detected with different antibodies by immunoblotting. Equal amounts of proteins from hemibrain homogenates of 17-mo-old WT, TRGL, Q175 and TRGL/Q175 (labeled as "Cross") were subjected to SDS-PAGE and processed for WB with different antibodies directed against HTT/mHTT, including MAB1574 (C1, C2), mAb PHP2 (C1) and MAB5490 (C2). Images were collected by a digital gel imager (Syngene G:Box XX9). The arrowhead and arrow (C2) depict a 120 kDa and a 48 kDa fragment, respectively. (C3) Densitometry was performed with Image J for the blots shown in (C2) and the results were normalized by the immunoblot(s) of given loading control protein(s) (e.g., GAPDH). Values are the Mean +/- SEM for each group (n = 7 TRGL, 4 Q175 and 10 TRGL/Q175). Significant differences among the groups were analyzed by One-Way ANOVA followed by Sidak's multiple comparisons test. * $P < 0.05$, ** $P < 0.01$.

Fig. 2. Colocalization of mHTT with p62, Ub and CTSD.

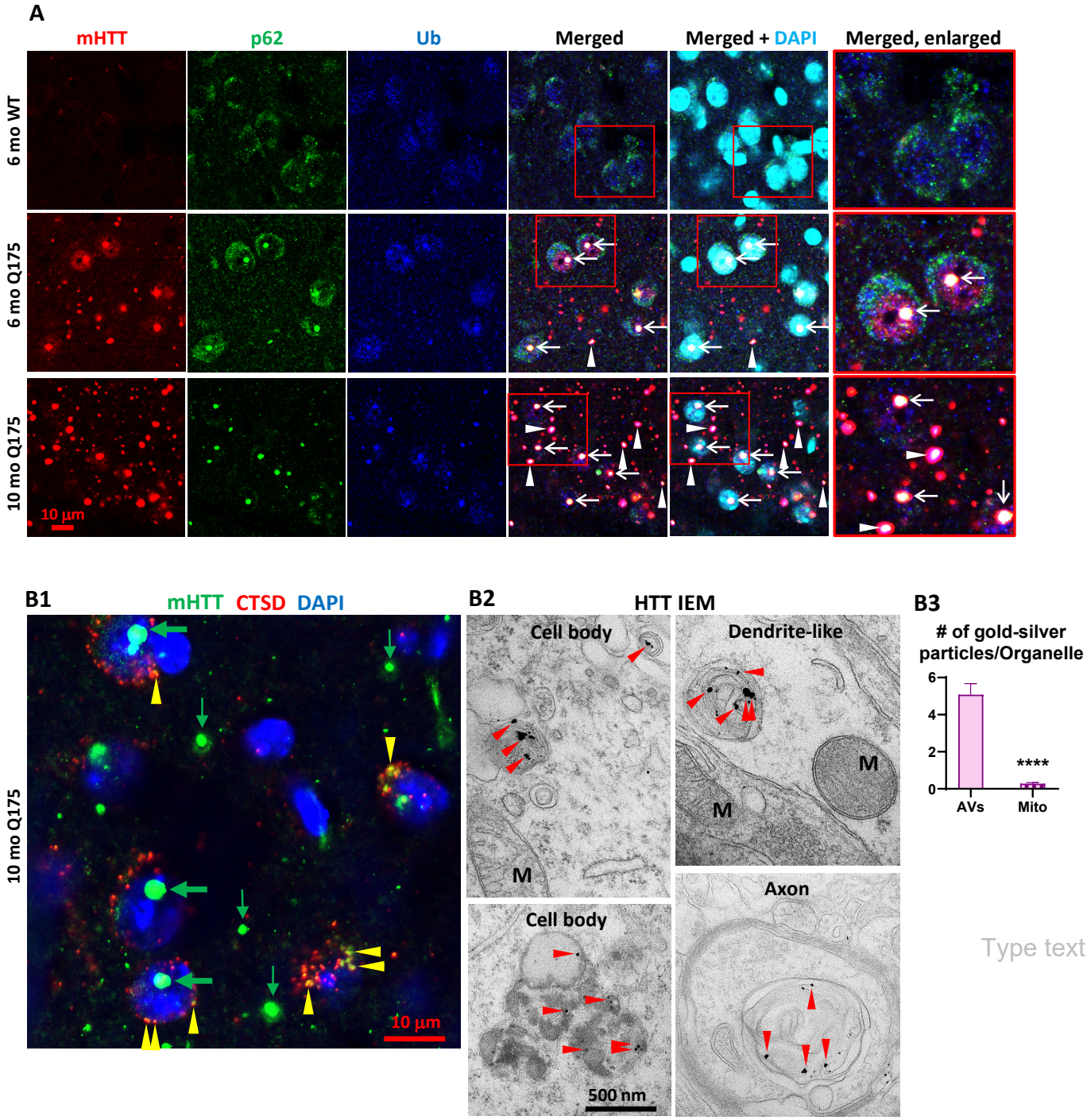

Type text he

Fig. 2 Colocalization of mHTT with p62, Ub and CTSD.

(A) Triple labeling detects colocalization of mHTT with both autophagy adaptor proteins p62 and Ub. Brain sections from 6-mo- and 10-mo-old mice were immunostained with antibodies to HTT (antibody MW8; red), p62 (green) or pan-Ub (blue), followed by an additional DAPI (cyan) labeling, and confocal images from the striatum are shown. Boxed areas are enlarged and shown in the last column. Arrows and arrowheads depict the white areas representing triply labeled inclusions containing the signals of the three proteins, where arrows are for NIIs, determined with the assistance from the nuclear DAPI labeling, while the arrowheads are for extranuclear inclusions. Bar = 10 μm.

(B) mHTT is detected in vesicles of the ALP. (B1) Brain sections from 10-mo-old Q175 were double-immunolabeled with antibodies to HTT (antibody MW8; green) and CTSD (red), followed by an additional DAPI (blue) labeling, and a 3-color-merged confocal image from the striatum is shown. Large and small green arrows depict HTT nuclear and extranuclear inclusions, respectively, while yellow arrowheads depict yellow puncta showing HTT and CTSD signal colocalization. Bar = 10 μm. (B2) IEM with anti-HTT antibody (MAB1574) specifically detects HTT signal, represented by the silver-enhanced gold particles (red arrowheads), in AV/LY in cell bodies, dendrites and axons. (B3) To demonstrate the labeling specificity of the HTT antibody in this IEM study, the number of silver-enhanced gold particles in AV/LY existing in neuronal cell bodies and neurites was counted from 69 EM images from two 10-mo-old Q175 mice against the number of silver-enhanced gold particles in mitochondria on the same images, and the result is shown in the bar graph. Statistical significances between the two groups were analyzed by unpaired, two-tailed t-test. **** $P < 0.0001$.

Fig. 3. Mild late-onset alterations in the ALP in the striatum of 17-mo-old Q175.

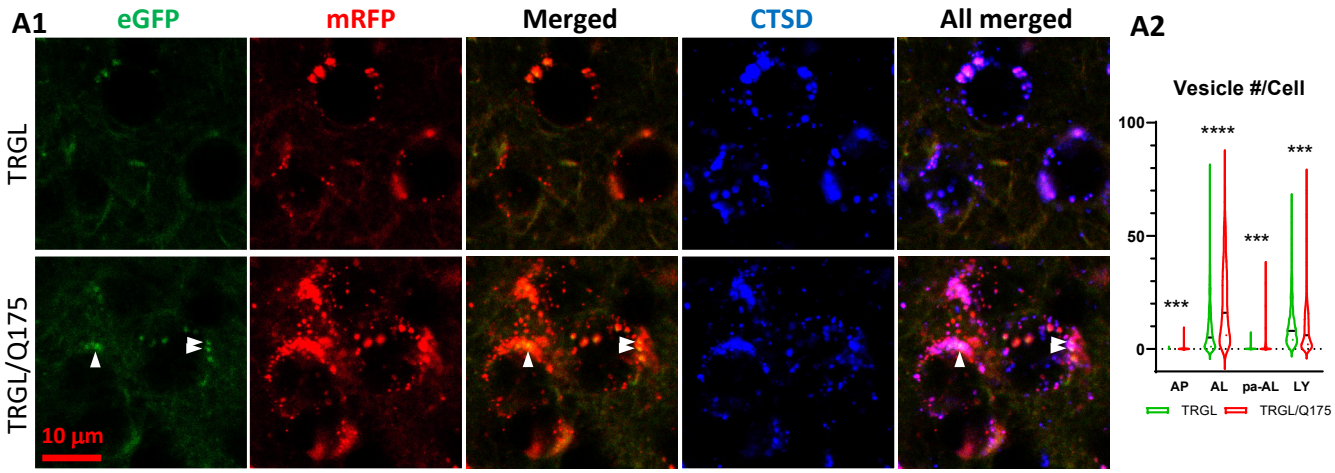

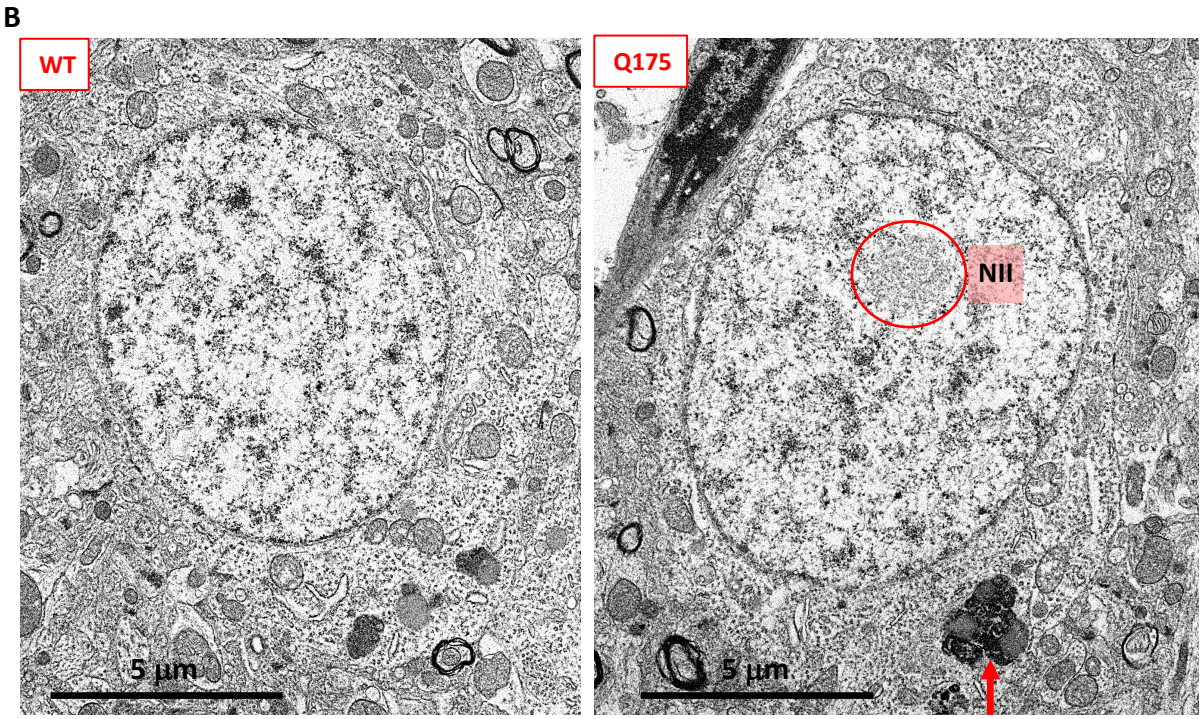

Fig. 3 Mild late-onset alterations in the ALP in the striatum of 17-mo-old Q175.

(A) Quantitation of AV/LY subtypes of striatal neurons detect increases in AL, pa-AL and a decrease in LY in 17-mo-old TRGL/Q175 vs. TRGL. (A1) Brain sections from TRGL and TRGL/Q175 (4 sections/mouse, 10 mice/genotype) were immunostained with an anti-CTSD antibody. Confocal images from the cranial-dorsal portion of the striatum (3 images at 120x/section) were collected and representative images for each eGFP-LC3 (green), mRFP-LC3 (red) and CTSD (blue) are shown. Arrowheads depict pa-AL. (A2) Hue angle-based analysis was performed for AV/LY subtype determination using the methods described in Lee et al., 2019. Data are presented as Vesicle #/Neuron (TRGL: n = 713 neurons; TRGL/Q175: n = 601 neurons). Statistical significances between the two groups for each vesicle type were analyzed by unpaired t-test. Two-tailed P value: *** $P<0.001$, **** $P<0.0001$.

(B) EM detects larger AL/lipofuscin granules in the Q175 striatum. Sagittal vibratome brain sections from 17-mo-old mice were cut and went through EM processing. Small blocks were obtained from the striatal area for ultrathin sectioning, followed by EM examinations of the grids. The red circle depicts NII, and the arrow depicts larger sized (> 1μm) lipofuscin granules, which were counted on randomly collected images of neurons from striatum of WT (420 neurons from n = 6 mice) or Q175 (586 neurons from n = 9 mice).

Fig. 4

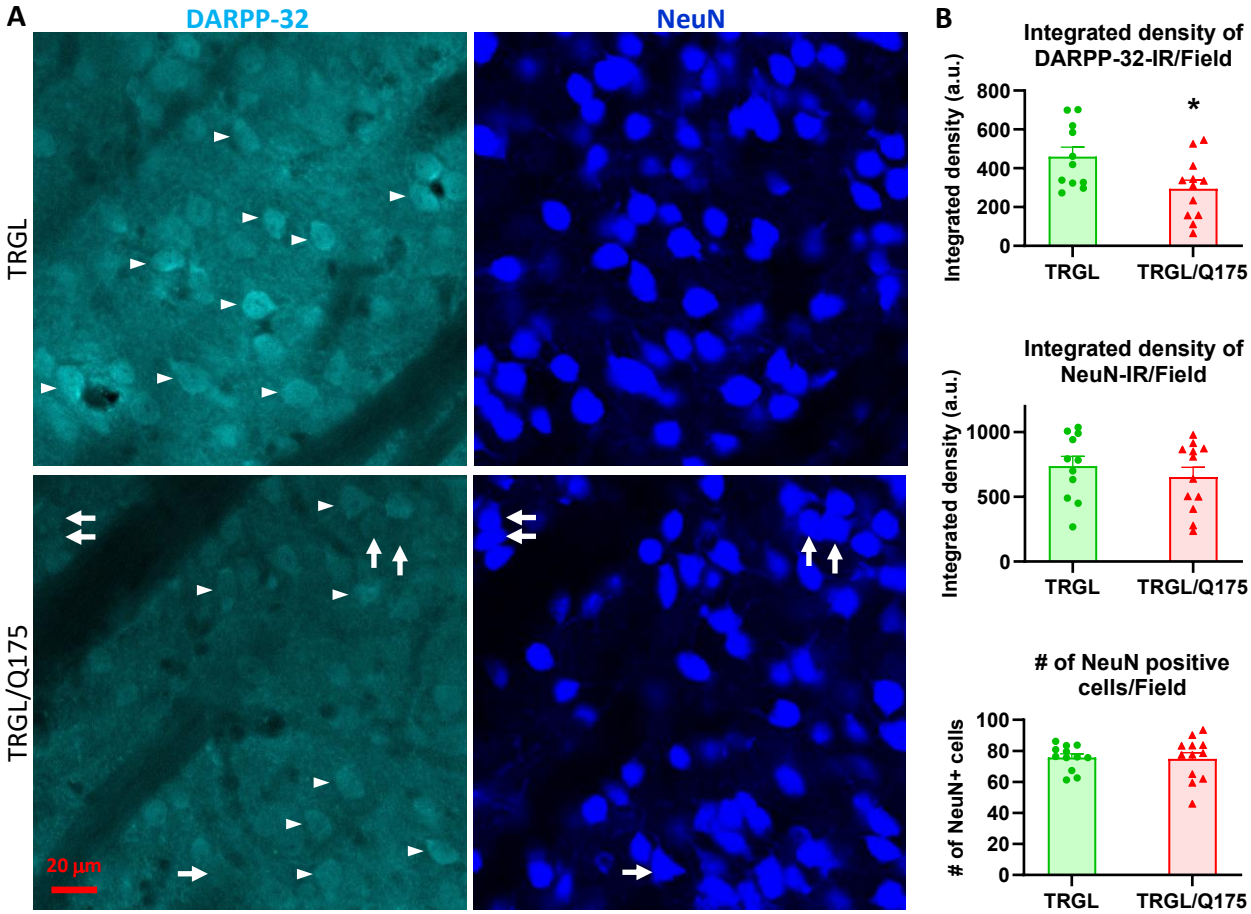

Fig. 4 Decrease of DARPP-32-IR in striatal neurons of 17-mo-old TRGL/Q175 in the absence of a NeuN signal reduction.

Brain sections from TRGL and TRGL/Q175 (n = 10 mice/genotype, 4 sections/mouse) were double-immunostained with anti-DARPP-32 and -NeuN antibodies. Confocal images from the cranial-dorsal portion of the striatum (3 images at 120x/section) were collected and representative images are shown (A). Arrows depict examples of neurons showing strong NeuN signal while minimal DARPP-32-IR. (B) Images were quantified by Image J for Integrated Density of DARPP-32- (top) or NeuN-IR/Image field (middle), and for # of NeuN positive cells/Image field (bottom). Statistical significances between the two groups were analyzed by unpaired, two-tailed t-test. * $P < 0.05$.

Fig. 5. mTORi INK exhibits target engagement and induces downstream responses in the ALP in 7-mo-old TRGL/Q175.

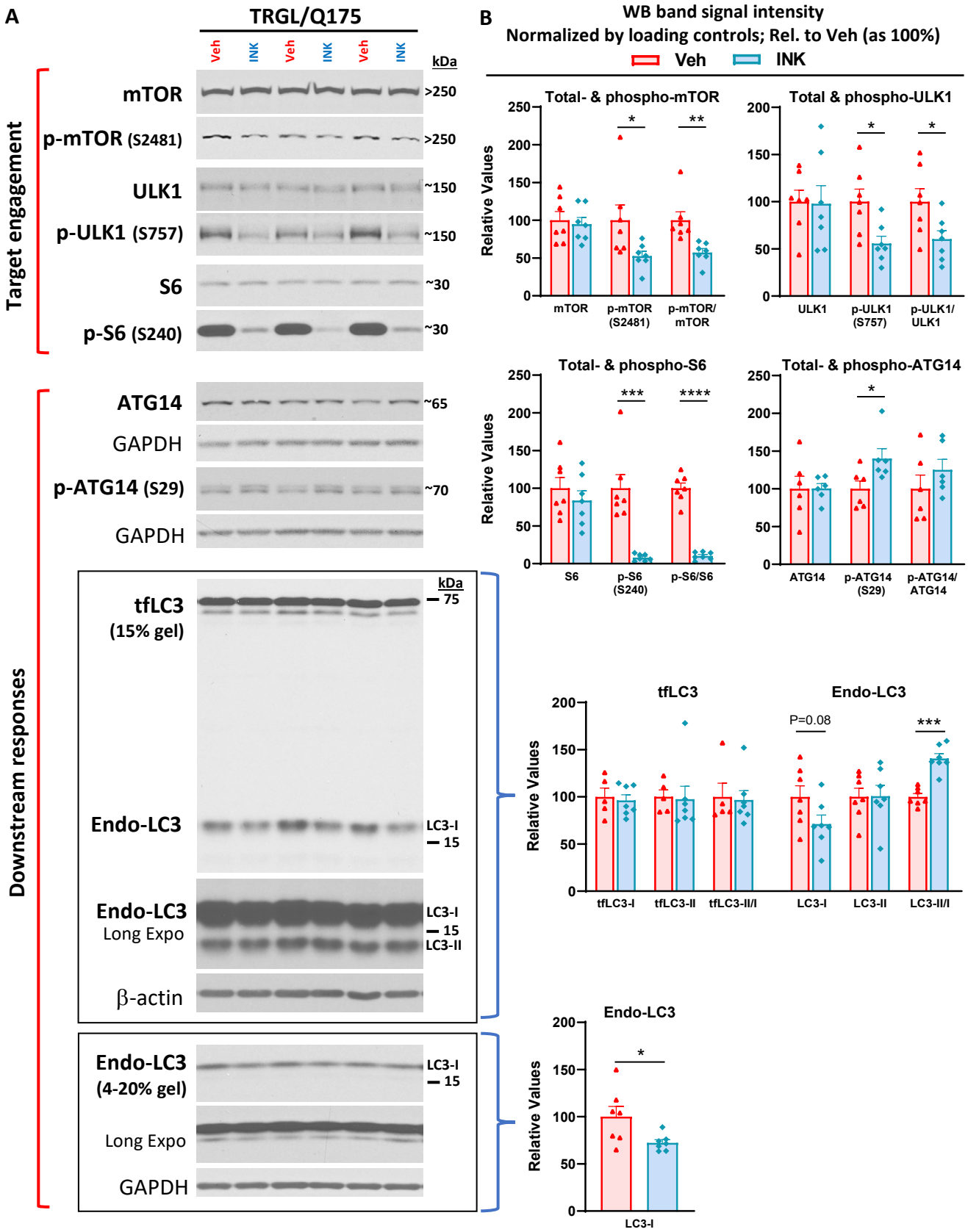

Fig. 5 mTORi INK exhibits target engagement and induces downstream responses in the ALP in 7-mo-old TRGL/Q175.

Equal amounts of proteins from brain homogenates of 7-mo-old TRGL/Q175 mice untreated (labeled as "Veh") or mTORi INK treated [4 mg/kg (4-mpk), daily, 3 weeks; labeled as "INK"] were subjected to SDS-PAGE and processed for WB with antibodies directed against several marker proteins in the autophagy pathway, representing target engagement of INK or downstream responses. Representative blots are shown on the left (A) while quantitative results of the blots are shown on the right (B). The bottom LC3 blots represent a repeated immunoblotting experiment. Values are the Mean +/- SEM for each group (n = 6-7 mice per condition). Significant differences between the two groups were analyzed by unpaired, two-tailed t-test. * $P<0.05$, ** $P<0.01$, *** $P<0.001$, **** $P<0.0001$. tfLC3 = mRFP-eGFP-LC3; Endo-LC3 = endogenous LC3.

Fig. 6

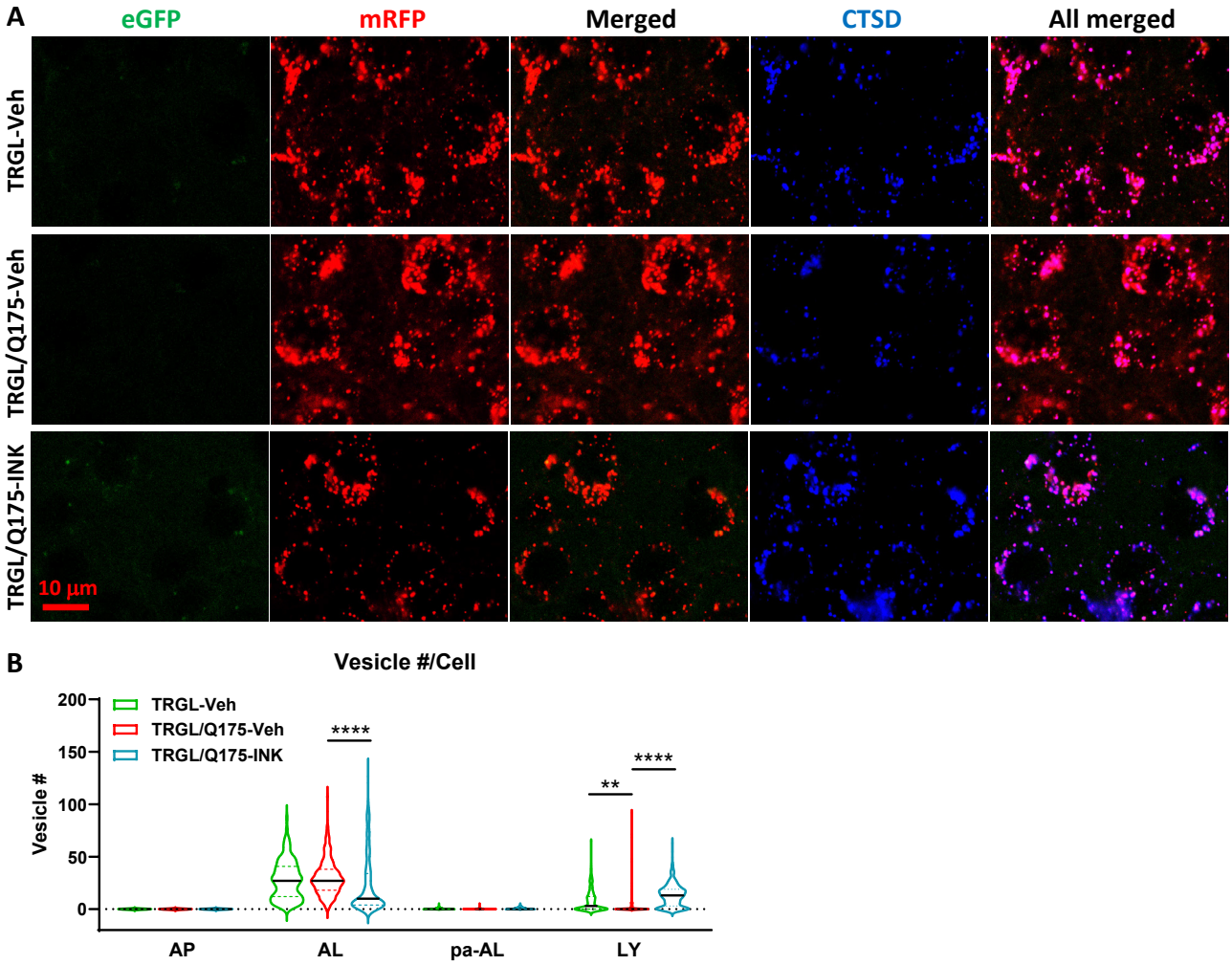

Fig. 6 mTORi INK reverses the mild alteration of AV/LY subtypes in the striatum of 7-mo-old TRGL/Q175.

(A) Brain sections from untreated or INK (4-mpk, 3w)-treated TRGL/Q175 vs. TRGL (4 sections/mouse, 5-6 mice per condition) were immunostained with an anti-CTSD antibody. Confocal images from the cranial-dorsal portion of the striatum (3 images at 120x/section) were collected and representative images for each eGFP-LC3 (green), mRFP-LC3 (red) and CTSD (blue) are shown. (B) Hue angle-based analysis was performed for AV/LY subtype determination using the methods described in Lee et al., 2019. Data are presented as Vesicle #/Neuron (TRGL-Veh: n = 260 neurons; TRGL/Q175-Veh: n = 218 neurons; TRGL/Q175-INK: n = 287 neurons). Statistical significances among the groups were analyzed by One-Way ANOVA followed by Sidak's multiple comparisons test. ** P<0.01, **** P<0.0001.

Fig. 7. mTORi INK reduces HTT-, Ub- or p62-IR-covered areas parallelly in the striatum of 7-mo-old TRGL/Q175.

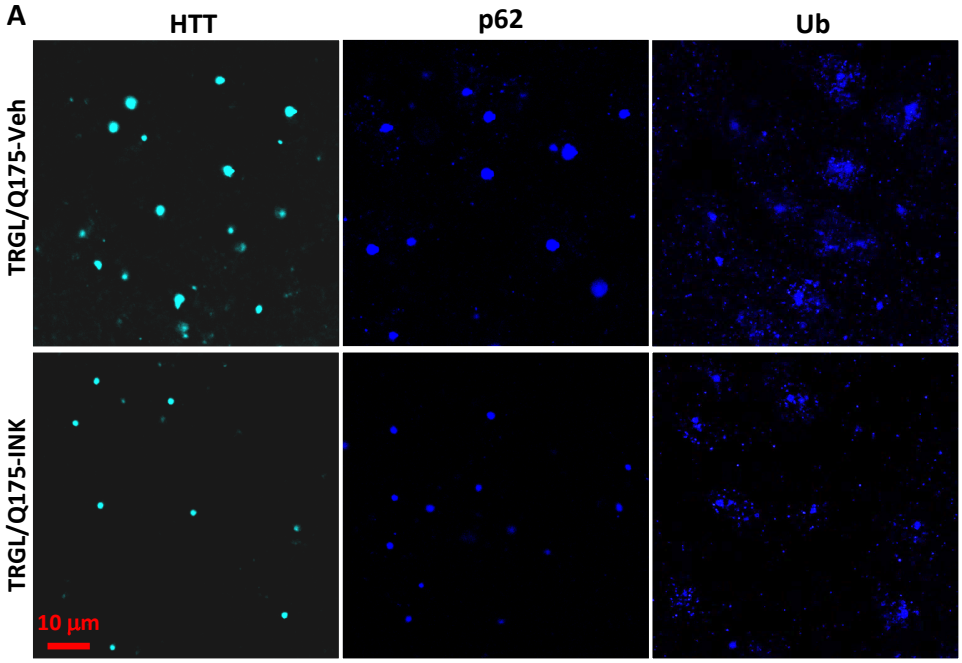

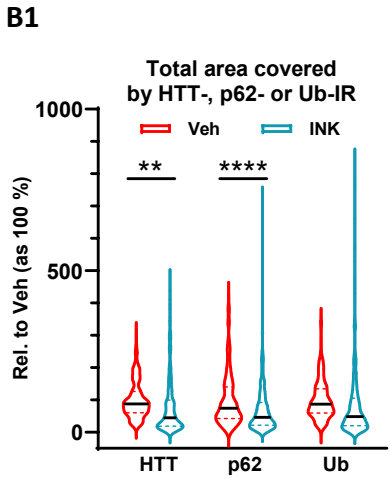

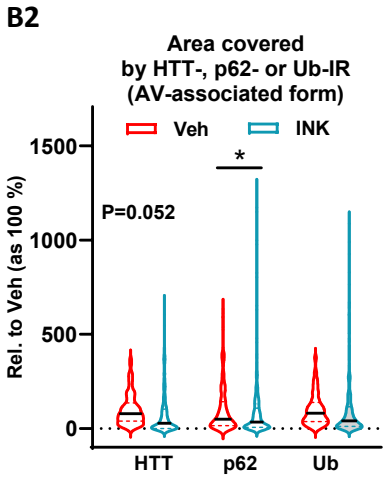

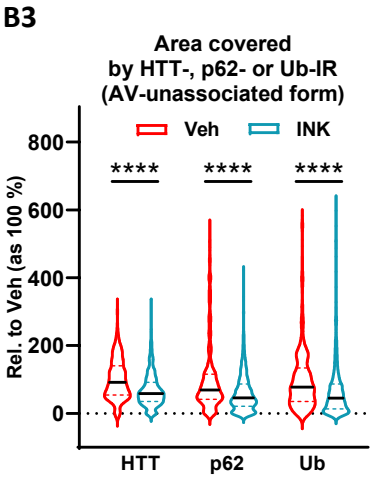

Fig. 7 mTORi INK reduces HTT-, Ub- or p62-IR-covered areas parallelly in the striatum of 7-mo-old TRGL/Q175.

(A) Brain sections from INK (4-mpk, 3w)-treated or untreated TRGL/Q175 (4 sections/mouse, 6-7 mice/condition,) were immunostained with anti-HTT (MW8), -p62 or -pan-Ub antibodies. Confocal images from the cranial-dorsal portion of the striatum (3 images at 120x/section) were collected. Shown are single-channel images (i.e., without showing the eGFP and mRFP signals). (B1-B3) Areas covered by either the HTT-, p62- or Ub-IR on a per cell basis are quantified (for HTT-IR, TRGL/Q175-Veh: n = 196 neurons, TRGL/Q175-INK: n = 385 neurons; for p62-IR, TRGL/Q175-Veh: n = 311 neurons, TRGL/Q175-INK: n = 378 neurons; for Ub-IR, TRGL/Q175-Veh: n = 244 neurons, TRGL/Q175-INK: n = 347 neurons) and grouped as "Total Area" (B1), "AV-associated Form" (i.e., the IR which was associated with tfLC3 signals representing AVs)(B2) or "AV-unassociated Form" (i.e., the IR which was not associated with the tfLC3 signals)(B3). Statistical significances between the two groups were analyzed by unpaired t-test. Two-tailed P value: * $P < 0.05$, **** $P < 0.0001$.

Fig. 8

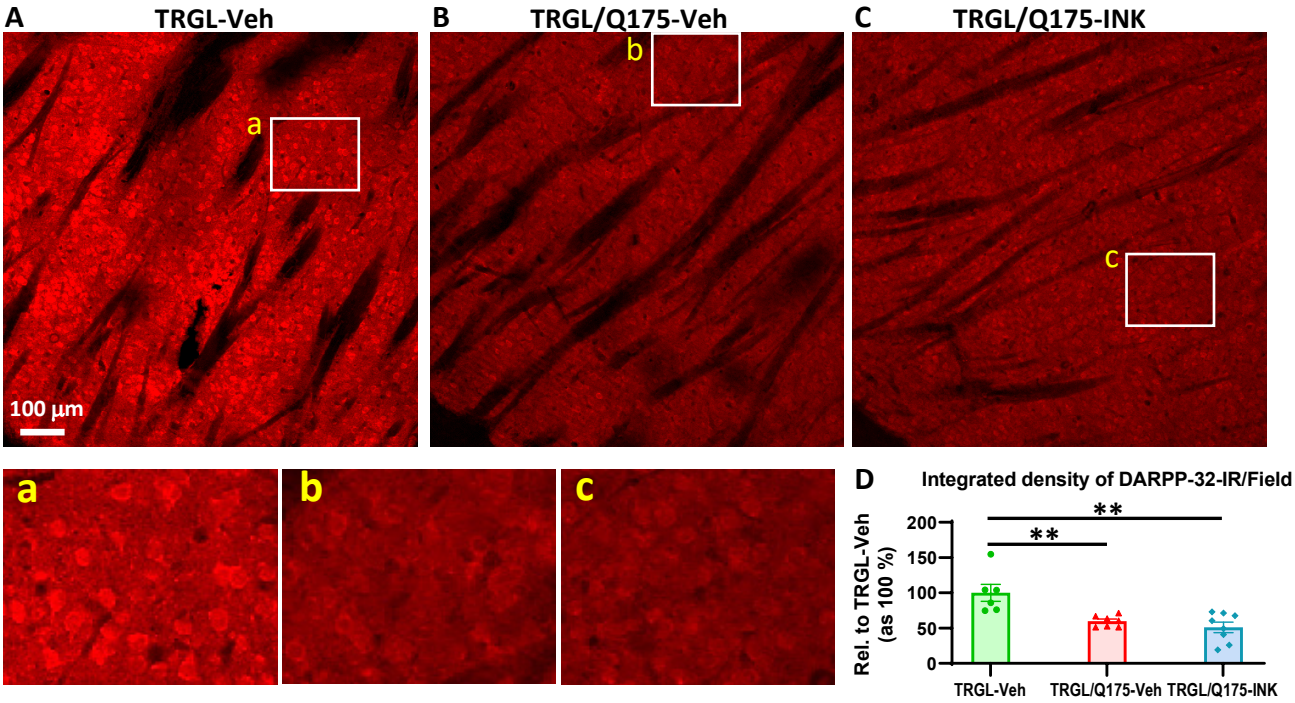

Fig. 8 INK treatment does not reverse the reduction of DARPP-32-IR in the striatum of 7-mo-old TRGL/Q175.

(A) Sagittal brain sections containing the striatum area were immunostained with an anti-DARPP-32 antibody, and 10x images taken from the cranial-dorsal portion of the striatum are shown (1st row). Boxed areas on the 1st row are enlarged and shown on the 2nd row for easy viewing of the immunostaining patterns for each condition. (B) For quantitation purpose, each whole 10x image (excluding the areas covered by the fiber bundles which usually exhibited minimal background staining – achieved by threshold setting) was quantified by Image J (1 image/section, 4 sections/mouse) and the results are expressed as the Integrated Density of DARPP-32-IR. n = 6-8 mice/condition. Statistical significances among the groups were analyzed by One-Way ANOVA followed by Sidak's multiple comparisons test. ** $P < 0.01$ compared to TRGL-Veh.

Fig. S1

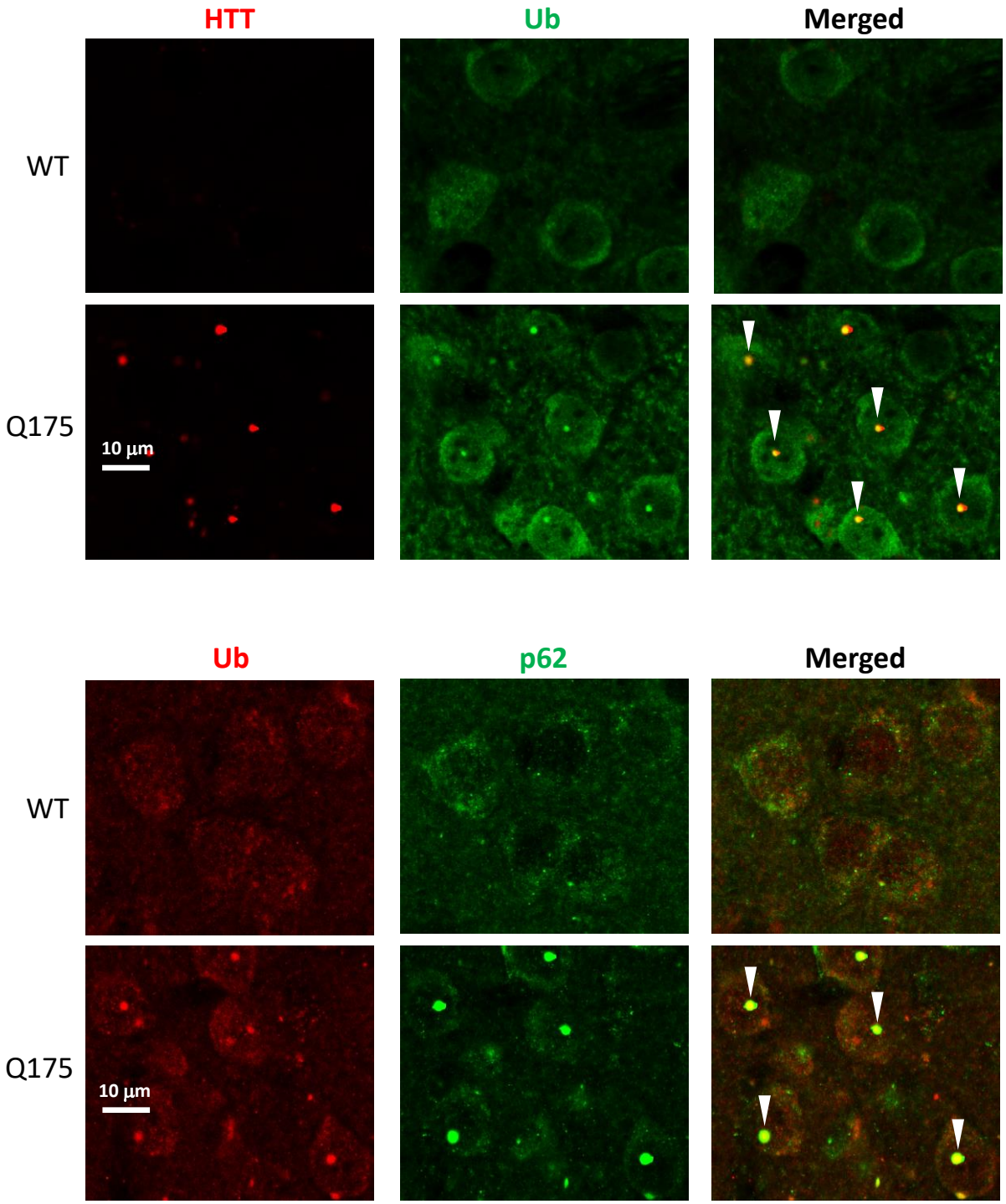

Fig. S1 (related to Fig. 2) Colocalization of HTT/Ub and Ub/p62 in IBs in the STR. Brain sections from 10-mo-old mice were processed for double IF with antibodies against HTT (antibody MW8; red) and pan-Ub (green), or pan-Ub (red) and p62 (green), and confocal images from the striatum are shown. Arrowheads depict IBs showing colocalization signals.

Fig. S2 (related to Fig. 3). Molecules involved in various stages of the ALP are largely unchanged in 17-mo-old TRGL/Q175.

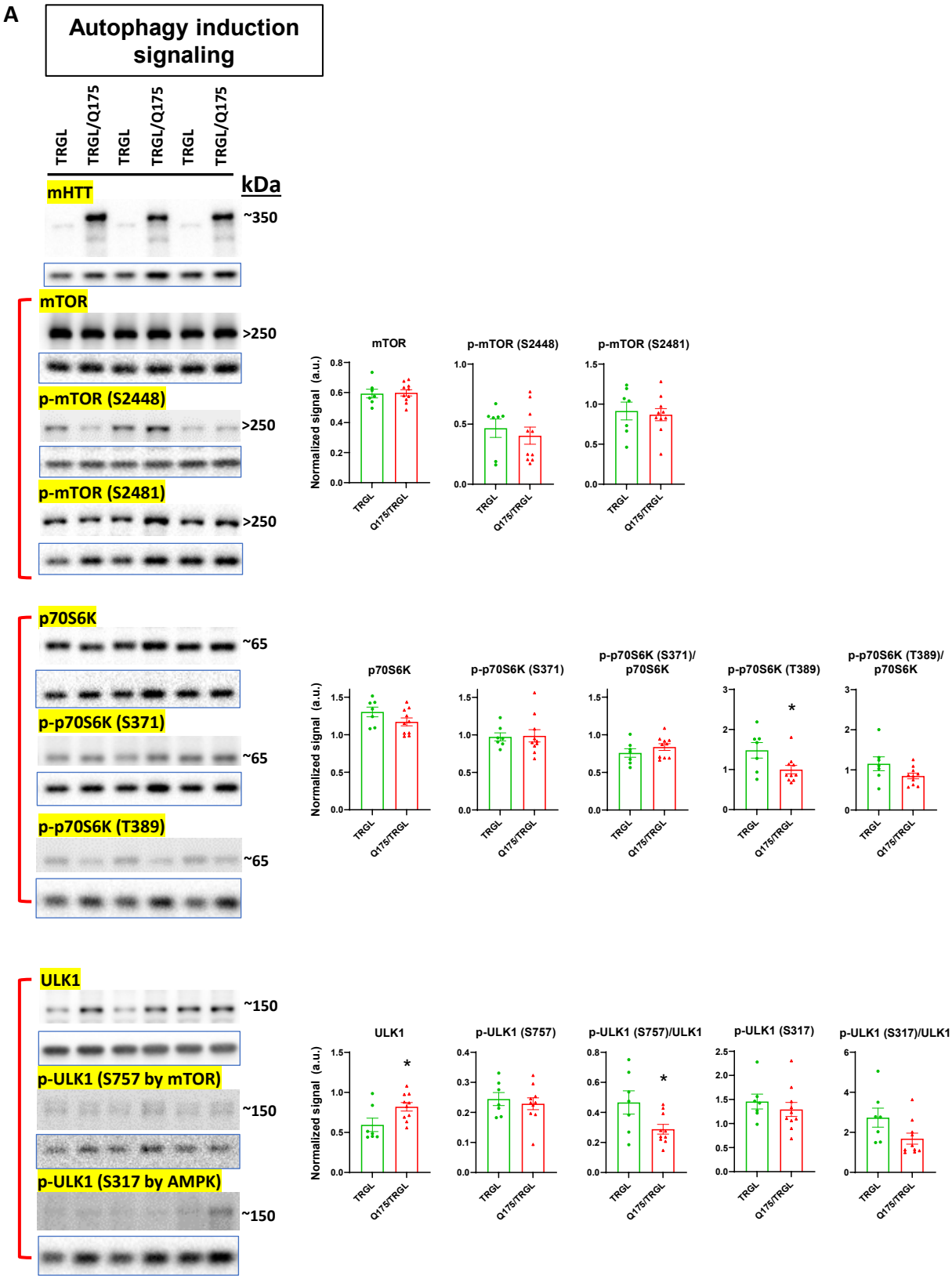

Fig. S2 (related Fig. 3). Molecules involved in various stages of the ALP are largely unchanged in 17-mo-old TRGL/Q175. (Cont'd)

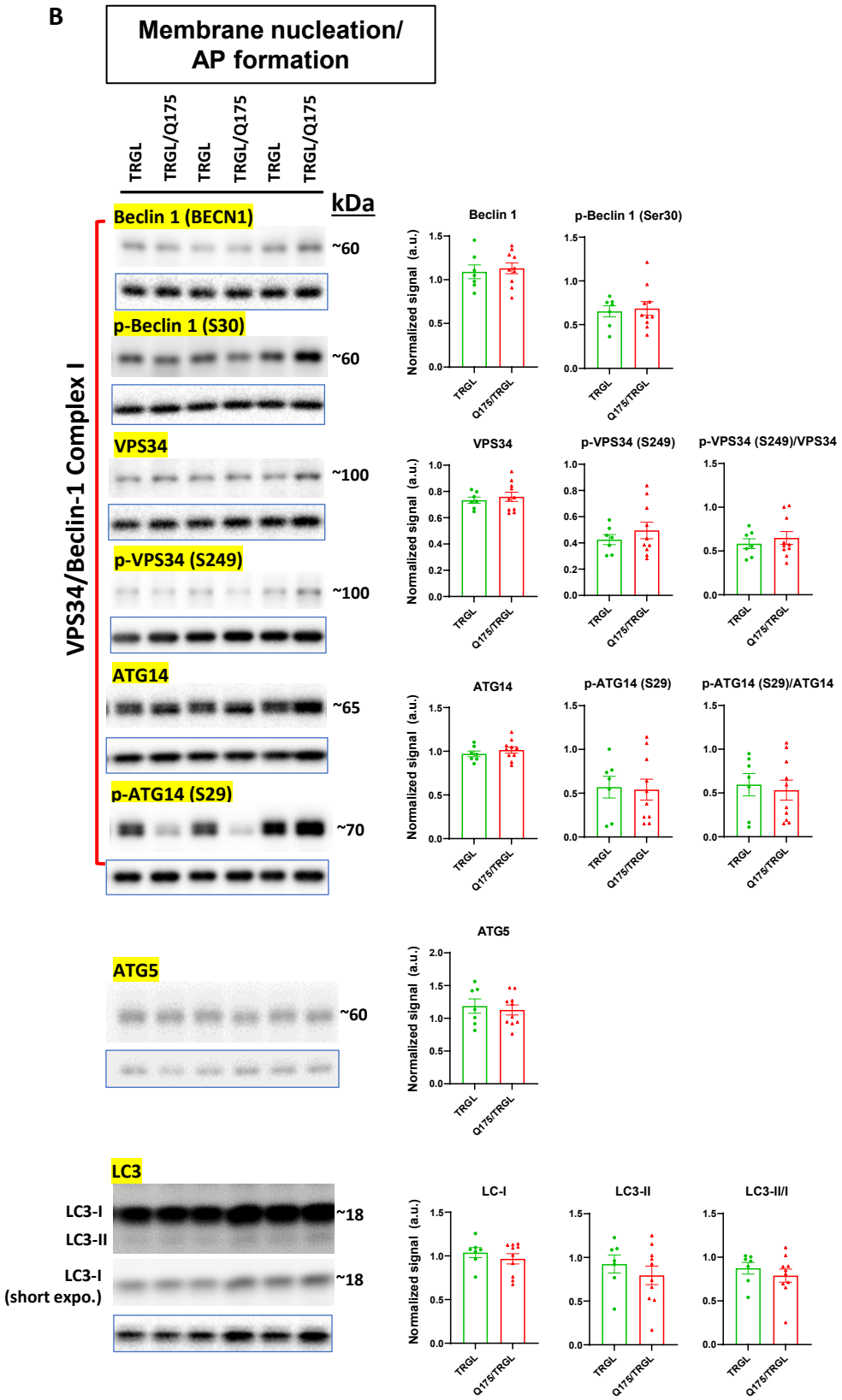

Fig. S2 (related to Fig. 3). Molecules involved in various stages of the ALP are largely unchanged in 17-mo-old TRGL/Q175. (Cont'd)

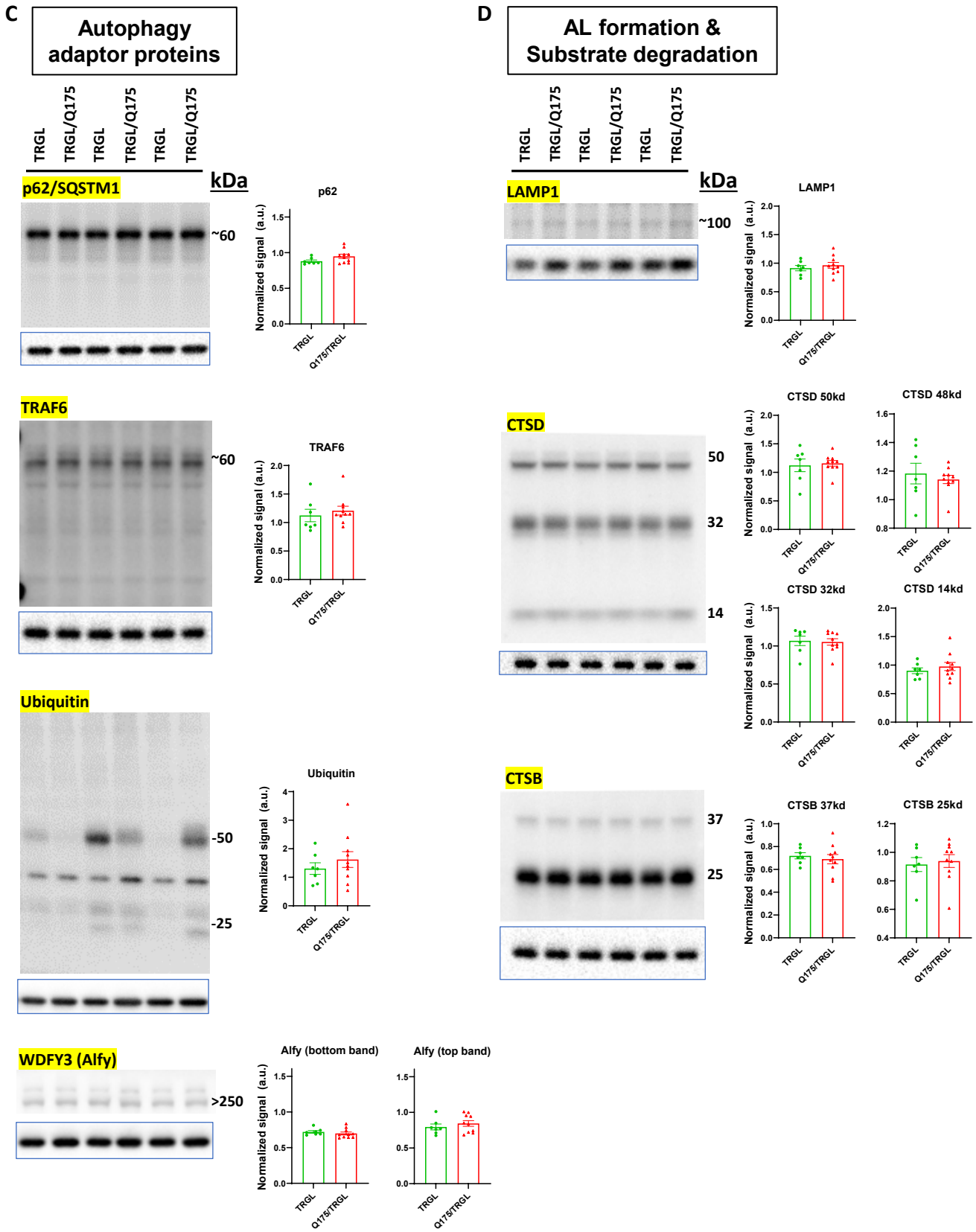

Fig. S2 (related to Fig. 3) Molecules involved in various stages of the ALP are largely unchanged in 17-mo-old TRGL/Q175.

Equal amounts of proteins from brain homogenates of 17-mo-old TRGL and TRGL/Q175 were subjected to SDS-PAGE and processed for WB with antibodies directed against a number of interested marker proteins in the ALP, grouped according to the functions of the proteins in the autophagy process: autophagy induction signaling (A), membrane nucleation/AP formation (B), autophagy adaptor proteins (C) and AL formation/substrate degradation (e.g., lysosomal hydrolases or structural components)(D). The blot of the loading control protein GAPDH is boxed and placed under each protein of interest. Images were collected by a digital gel imager (Syngene G:Box XX9). Densitometry was performed with Image J and the result for each protein of interest was normalized by its corresponding GAPDH blot and presented in the bar graph. Values are the Mean +/- SEM for each group (n = 7 TRGL and 10 TRGL/Q175). Significant differences between the 2 groups were analyzed by unpaired, two-tailed t-test. * $P < 0.05$, ** $P < 0.01$, *** $P < 0.001$.

Fig. S3 (related to Fig. 5). Dosing tests demonstrate mTORi INK BBB penetration and target engagement even at low dosages.

A

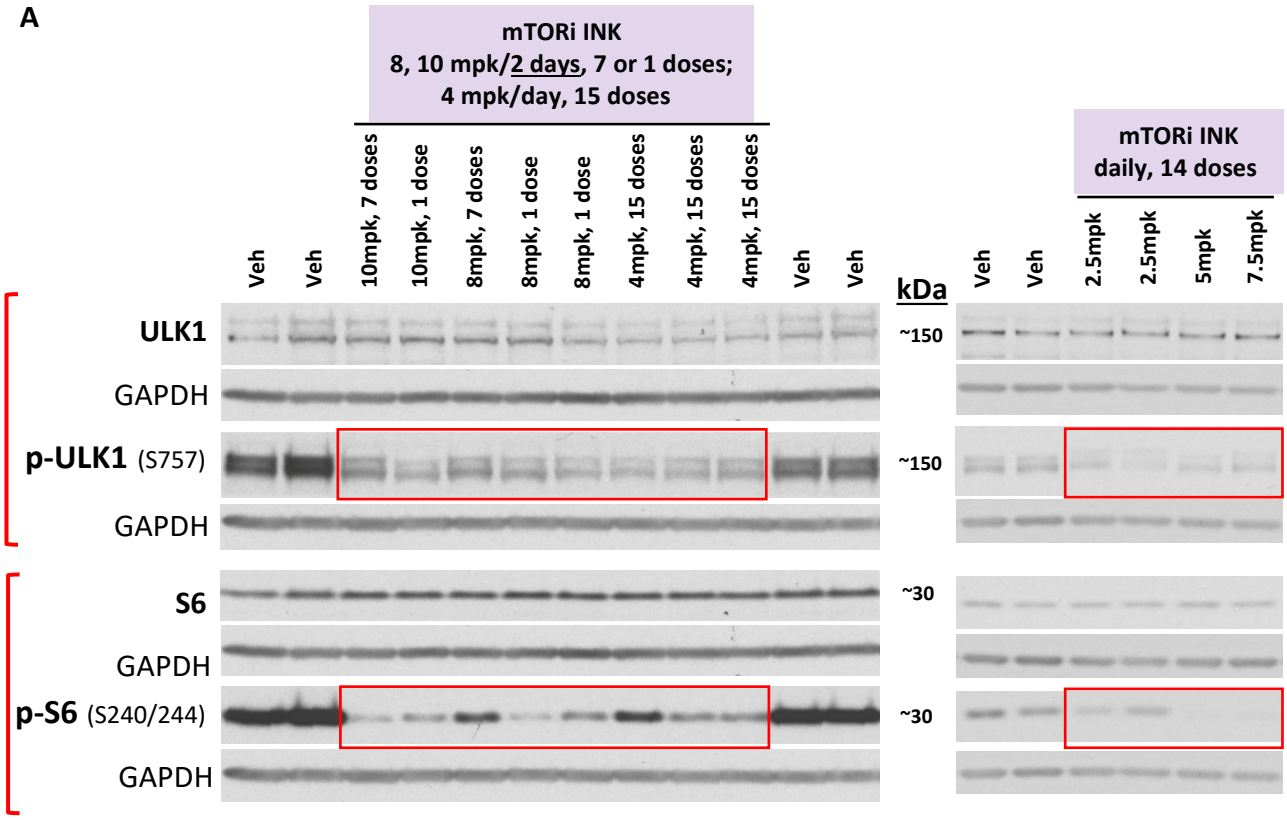

B

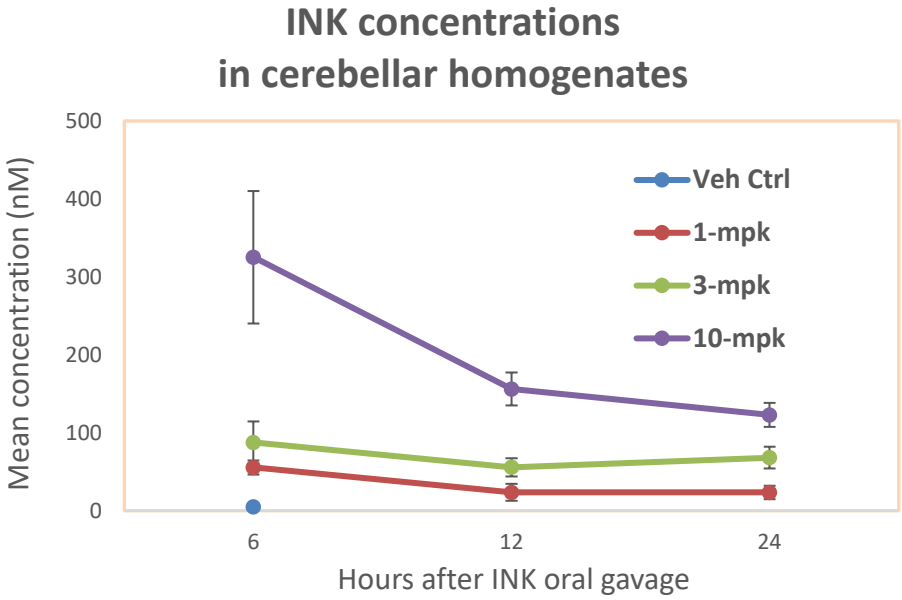

Fig. S3 (related to Fig. 5) Dosing tests demonstrate mTORi INK BBB penetration and target engagement even at low dosages.

(A) Dosing tests for INK. INK or the vehicle was administered by oral gavage. Two dosing tests were done in 6-mo-old WT mice, one with 10, 8 mg/kg (mpk) every other day or 4-mpk daily for 2 weeks and the other with 7.5, 5, 2.5-mpk daily for 2 weeks. Equal amounts of proteins from brain homogenates of mice receiving vehicle (labeled as "Veh") or INK were subjected to SDS-PAGE and processed for WB with antibodies directed against marker proteins representing target engagement of INK, such as p-ULK1 (S757) and p-S6 – the drug effects are reflected by the changes within the boxed areas compared to the signals of Veh outside the boxed areas.

(B) INK was detected in the brains of mice receiving a single dose via oral gavage. After 6, 12 or 24 hrs post INK administration to 6-mo-old WT mice, INK was detected in cerebellum of mice treated with 1, 3 or 10-mpk INK. Total 60 mice: n = 6 mice/dose/time point, where the Vehicle control group was just tested once at the 6-hr time point.